Evaluation of the Advanced Collapsed-cone Engine for High Dose Rate Ir-192 GYN and Scalp Brachytherapy

by

Brie Claire Cawston-Grant

A thesis submitted in partial fulfillment of the requirements for the degree of

Master of Science

in

Medical Physics

Department of Oncology

University of Alberta

Abstract

Standard treatment planning in brachytherapy (BT) uses the well-accepted TG-43 dose calculation formalism, which does not account for tissue or material heterogeneities. However, recent developments in BT have led to commercial treatment planning systems (TPSs) using model based dose calculation algorithms (MBDCAs), and their introduction requires critical evaluation before clinical implementation. MDBCAs consider tissue and medical accessory composition, and therefore they have the potential to improve dose calculation accuracy. The work presented in this thesis investigates the performance of the Advanced Collapsed-cone Engine (ACE) in Oncentra® Brachy v4.5 (Elekta, Stockholm, Sweden) for two types of high-dose-rate brachytherapy treatments that have not yet been investigated by others: gynecological treatments using a multi-channel vaginal cylinder (MCVC) applicator, and treatments of non-melanoma skin cancers (NMSC) of the scalp. The evaluation of ACE was performed by comparing ACE dose calculations to radiochromic film measurements in clinically relevant phantoms.

For the MCVC experiments, the TG-43 formalism was used to prescribe 500 cGy to the surface of the applicator. Film measurements were made at the applicator surface in a water tank. When the central channel of the applicator was used, the film measurements showed a dose increase of (11 ± 8)% (k=2) above two outer grooves on the applicator surface. This increase in dose was confirmed with the high accuracy mode ACE calculations (hACE), but was not confirmed with the standard accuracy mode ACE calculations (sACE) at the applicator surface. Additionally, a baseline dose variation of (10 ± 4)% (k=2) of the mean dose was measured azimuthally around the applicator surface. This variation was not confirmed with either sACE or hACE. When the peripheral channels were used, a periodic azimuthal variation in measured dose was observed around the applicator. The sACE and hACE calculations confirmed this variation and agreed within 1% of each other at the applicator surface.

A tissue equivalent slab phantom was designed to model variable heterogeneities that are present in scalp BT treatments: air gaps between the mold and skin, skin thickness, and skull thickness. ACE dose calculations were assessed for six variations of this phantom. Radiochromic film measurements were performed at four different depths within the phantoms, and were compared to the ACE calculations, which used computed tomography images of the phantoms. The TG-43 and hACE calculations were found to overestimate the dose below the skull layer by an average of (8 ± 2)% and (9 ± 3)%, respectively. This underestimation of attenuation through the skull most likely results from the ACE algorithm's use, in non-water material, of photon scatter spectra generated using Monte Carlo simulations in water, rather than spectra generated within the material itself.

Overall, this work has identified attributes of the ACE algorithm that should be considered if it is used in similar clinical situations.

Preface

Computed tomography images of skin cancer patients were used with ethics approval by the Health Research Ethics Board of Alberta (HREBA) Cancer Committee, Project Name: "Preclinical evaluation of heterogeneity corrections in brachytherapy treatment planning," Project Number: HREBA.CC-16-0657, August 30th/2016.

Components of Chapter 3 were published as the conference abstract: B. Cawston-Grant, H. Morrison, G. Menon, R.S. Sloboda, "Evaluation of the surface dose around a multi-channel vaginal cylinder applicator using radiochromic film and ACE algorithm" *Brachytherapy,* vol. 15, Suppl 1, S89-S90. Components of Chapter 4 were published as the conference abstract: B. Cawston-Grant, H Morrison, R.S. Sloboda, G. Menon, "Investigation of the Advanced Collapsed-cone Engine for HDR brachytherapy scalp treatments," *Medical Physics,* vol. 43, issue 8, 4936. I was responsible for the data collection and analysis as well as abstract composition. H. Morrison assisted with data collection and manuscript edits. G. Menon and R.S. Sloboda were the supervisory authors and were involved in concept formation and manuscript composition. The Monte Carlo simulations presented in Chapter 3 were performed by H. Morrison.

Acknowledgements

It is with sincere gratitude that I thank my supervisors Dr. Geetha Menon and Dr. Ron Sloboda. Their encouragement and expert guidance made this degree not only possible, but enjoyable. They trusted in my abilities, listened to my ideas, and cared about my future – I couldn't have imagined a more thoughtful team to work with.

I am also very appreciative of my supervisory committee members Dr. Gino Fallone and Dr. Don Robinson for their direction and advice, as well as my "arms-length" examiner Dr. Hans-Sönke Jans.

My further thanks and appreciation to:

- Dr. Hans-Sönke Jans for his assistance in obtaining the micro-CT images, and the Wuest group at the Cross Cancer Institute for providing access to the micro-CT scanner.
- Yuri Niatsetski and Bob van-Veelen from Elekta for their advice on the use of ACE.
- Shima Yaghoobpour Tari for helping me obtain the CT scans, and Hali Morrison for teaching me about film and discussing brachytherapy.
- The CCI machine shop staff for constructing the applicator mount and sleeve for the gynecological experiments, and for brightening the department with their positivity and senses of humor.

Lastly, I am sincerely grateful to my parents and family for their kind words and constant support.

List of Figures

List of Tables

List of Abbreviations

AAPM	American Association of Physicists in Medicine
ACE	Advanced Collapsed-cone Engine
BT	Brachytherapy
CAX	Central AXis
CCD	Charged-Coupled Device
CCSC	Collapsed-Cone Superposition Convolution
CPE	Charged Particle Equilibrium
CT	Computed Tomography
CTV	Clinical Target Volume
EBRT	External Beam Radiation Therapy
EV	Effective Variance
GBBS	Grid Based Boltzmann Solver
hACE	High accuracy ACE
HDR	High Dose Rate
I-125	Iodine-125
ICRU	International Commission on Radiation Units and measurements
Ir-192	Iridium-192
IS	Inverse Square
KERMA	Kinetic Energy Released per MAss
LDR	Low Dose Rate
LiPCDA	Lithium PentaCosa-10, 12-Diynoic Acid
MC	Monte Carlo
MCVC	Multi-Channel Vaginal Cylinder
MDBCA	Model Based Dose Calculation Algorithm
MR	Magnetic Resonance
NIST	National Institute of Standards and Technology
NMSC	Non-Melanoma Skin Cancer
OAR	Organ At Risk
OcB	Oncentra® Brachy
Os-192	Osmium-192
PDR	Pulsed Dose Rate
Pt-192	Platinum-192
RT	Radiation Therapy
sACE	Standard accuracy ACE
SCERMA	SCattered Energy Release per MAss
TG-186	Task Group #186
TG-43	Task Group #43
TPS	Treatment Planning System
VC	Vaginal Cylinder
WAFAC	Wide Angle Free Air Chamber
μCT	Micro-CT

Table of Contents

Chapter 1 – Background and Thesis Outline

1.1 – Introduction

Radiation therapy is generally not the first treatment that comes to mind when one speaks of cancer, but despite its lack of public spotlight, it is essential to achieve tumor control or effective palliation for about 50% of all patients (1). The modality of radiation therapy is as diverse as the patients it treats – radiation type, radiation energy, the shape of the treatment beam, radiation source intensity, and how the radiation is produced are selected based on the shape, size, location, and aggressiveness of the cancer. Brachytherapy ("short distance" therapy, BT) is the treatment of cancer by placing a radiation source in close proximity to the tumor. For a variety of reasons, the sophistication of treatment planning software for brachytherapy has lagged behind that of its counterpart, external beam radiation therapy (EBRT). Treatment planning dose calculations for EBRT take into account the varying composition of human tissues and medical accessories, whereas BT dose calculations do not. Radiotherapy equipment suppliers have recently addressed this deficiency with new algorithms that can incorporate material heterogeneities into radiation dose calculations. Will these Model Based Dose Calculation Algorithms (MBDCAs) increase the accuracy of brachytherapy dose calculations, thereby improving the treatment outcomes of cancer patients? The answer lies at the end of rigorous commissioning of the MBDCAs through theoretical and experimental means, followed by assessment of their performance and necessity in clinical practice by the medical physics and physician community.

1.2 – Radiation Therapy

1.2.1 – Brachytherapy and External Beam Treatments

On November 17th 1903, Dr. Margaret Cleaves published the first claim for the use of radium for cancer treatment in the United States (2). She used sealed glass tubes of radium for treatment of advanced squamous cell carcinoma of the cervix, and for recurrent carcinoma of the scalp.

Brachytherapy was the first modality of radiation therapy, but with the advent of Cobalt-60 EBRT and medical linear accelerators (linacs) in the 1950's, brachytherapy became the lesser used modality. Linacs are able to produce deeply penetrating beams that can more easily treat cancers within the body (2). The decrease in BT utilization has continued, particularly for cervical cancer treatments. For example, between 2002 and 2003 there was a 23% decrease in its use in the United States for cervical cancer treatments (3). This recent decrease has been attributed to adoption of highly conformal EBRT techniques, potentially due to the influence of Medicare re-imbursement (3). This decline is concerning as evidence has increased for BTs importance in achieving optimum patient outcomes (4).

Cancer sites that are treated with brachytherapy benefit from the sharp dose fall-off away from the BT source, which allows for the sparing of organs at risk (OARs), the ability to create a highly conformal dose distribution despite difficult anatomical geometries, and the flexibility to tailor the source strength and energy to the treatment. Currently, BT is used to treat many cancers, including head and neck, gynecological, prostate, bronchus and esophageal, breast, rectal, ocular, and skin cancers.

The two types of BT treatments investigated in this thesis are for gynecological cancers, and for non-melanoma skin cancers (NMSC) of the scalp. In a study by Han *et al*.(3), the efficacy of BT for cervical cancer treatments was made very clear. Their analysis of the surveillance, epidemiology, and end results database for cancer patients diagnosed between 2000 and 2009 with stage 1B-IVA cervical cancer found a significant improvement in survival when BT was used in treatment. The use of BT for NMSC is relatively new and therefore is not supported by large trials. However, the ability to achieve a conformal dose and to decrease the number of treatment fractions lends to BT being ideal for certain scalp treatments (5).

1.2.2 – Brachytherapy Sources and Delivery

BT treatments can be classified in numerous ways such as by the characteristics of the treatment method and by source characteristics. The treatment methods can be categorized as follows: intracavitary, where a BT applicator is used to guide the source into an anatomical cavity; interstitial, where BT applicators or sources are placed directly into the tissue; intraluminal, where BT applicators are inserted into a lumen of the body (e.g. esophagus); intravascular, where applicators are inserted in arteries for the treatment of restenosis (artery narrowing) (6).

Sources that can be used for BT treatments are restricted by practical considerations such as size, cost, and handling ability. Whether a source is suitable for a particular treatment site is determined by the type of radiation emitted (photons or electrons), the spectrum of emitted energies, and its physical half-life (for radio-nuclides). Permanent seed implant treatments, such as for prostate cancer, most commonly utilize Iodine-125 (I-125) seeds, which produce low energy x-rays (28 keV average energy) and have a half-life of 60.2 days. The low energy of I-125 photons allows for easier radiation protection and reduced exposure to the public, while the half-life is convenient for shipping purposes. Permanent implant treatments are classified as low dose rate (LDR), where the dose rate is usually between 0.5 and 1 Gy/hr. The International Commission on Radiation Units and measurements (ICRU) defines the upper limit of LDR to be 2 Gy/hr (7). On the other end of the dose rate spectrum are high dose rate (HDR) treatments, which have the benefit of decreased treatment time due to the higher source strength of the radionuclide. HDR treatments are defined to have dose rates greater than 0.2 Gy/min and are typically delivered at a dose rate close to 2 Gy/min. Iridium-192 (Ir-192) is the source most commonly used for HDR treatments. Pulsed dose rate (PDR) treatments also use an Ir-192 source. PDR is typically used to treat cervical cancer, and delivers treatment for part of every hour over a total treatment time period equal to that for LDR. PDR is advantageous because it allows for a remote afterloading machine to be used, while maintaining the radiobiological benefits of LDR treatments (6).

Prior to the 1960's the majority of BT sources and applicators were inserted into the patient manually. Remote afterloading was first proposed in 1964 at the Memorial Sloan Kettering Cancer Center (2). It involves the movement of a remotely controlled single source, via a drive cable, from a shielded machine into catheters or channels that are inside or on the surface of the patient. The source dwells in different positions in the channels in an applicator to simulate multiple sources delivering dose. A modern Nucletron microSelectron HDR remote afterloader (Elekta, Stockholm, Sweden) is illustrated in Figure 1.1.

The term applicator in BT refers to a device that guides the source into the patient in a way that achieves the desired dose distribution. Gynecological applicators, such as the tandem and ring applicator (Figure 1.1), are inserted into a woman's vagina and/or uterus for the treatment of vaginal, cervical, or endometrial cancer. Guide or transfer tubes connect the afterloader to an applicator, allowing for the source to travel in specific channels of the applicator. Applicators also include devices used to treat skin cancers. For example, Elekta's Leipzig applicators consist of a single catheter/channel that enters a tungsten cone. The cone is placed over the lesion, shielding surrounding skin, and the source dwells inside the cone. Surface applicators can also be custom made for individual patients using wax and plastic catheters. At our clinic, NMSCs of the scalp are treated using HDR BT and customized applicators. The applicator is created by first making a mould of the patient's head with a mouldable plastic, adding a wax bolus overtop the region covering the tumor, then adhering catheters to the wax bolus.

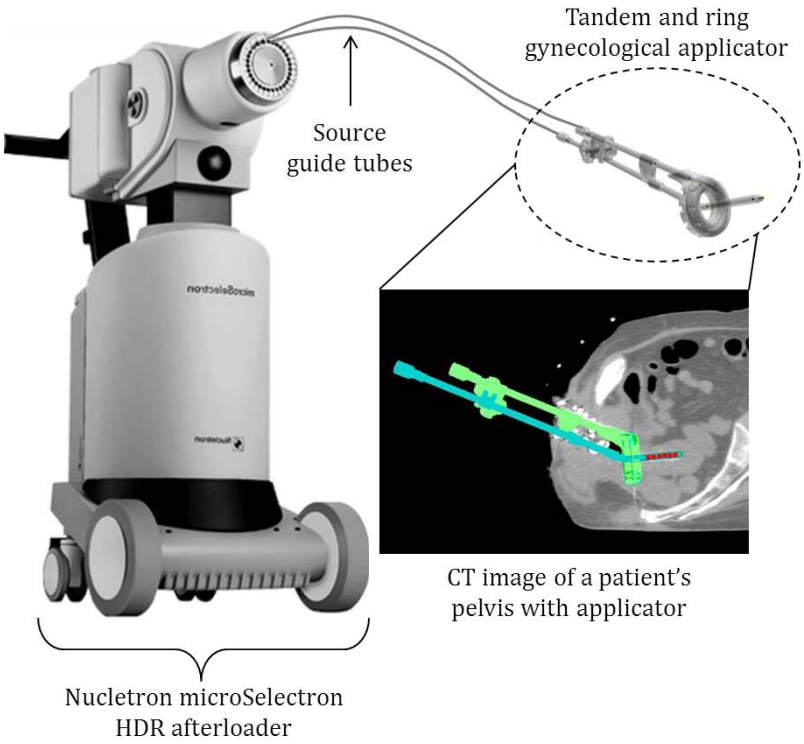

Figure 1.1– The Nucletron microSelectron HDR afterloader connected to a tandem (blue, extending into uterus) and ring (green, against cervix) applicator (Elekta, Stockholm, Sweden). Six dwell positions (red dots) are activated in the tandem.

1.3 – Brachytherapy Treatment Planning and Dose Calculation

Following cancer diagnosis, via use of physical exam, pathology, and imaging modalities, the process of BT generally involves the following steps: (i) either computed tomography (CT) or MRI simulation is performed to image the applicator position with respect to the anatomy of the patient; (ii) the images are then imported into the treatment planning system (TPS), and the tumor and OARs are delineated by the physician; (iii) source dwell times, which obtain the desired dose to the tumor while sparing the OARs, are determined; (iv) the treatment is delivered to the patient based on the determined dwell times (8). Current BT dose calculations, which are based on the superposition of the products of single-source dose distributions and source dwell times, use the well accepted TG-43 formalism (discussed in more detail in Chapter 2). TG-43 calculations assume

all materials in the treatment applicator and the patient are composed of water. This assumption is clearly inaccurate, especially for treatments in close proximity to bone or air, and for treatments that use non-water-equivalent applicators to guide the source into the patient.

Assuming all materials are composed of water has the potential to introduce errors in dose calculations (9–11). The consideration of tissue heterogeneities for Ir-192 treatments has been reported to yield dose differences of up to 5% in the presence of air and cortical bone (12). In clinical practice, this difference may be critically important in cases where OAR doses are allowed to rise to their upper limit when trying to achieve acceptable target coverage, a common occurrence. Consequently, calculating OAR doses accurately might be the difference between successful OAR sparing and a radiation-related OAR complication. In addition, neglecting attenuation when using metallic applicators can overestimate the dose by up to 3.5% for Ir-192 brachytherapy (9). The possibility of improving the accuracy of treatment planning in BT has led to the development of MBDCAs for this application.

1.3.1 – Model Based Dose Calculation Algorithms

1.3.1.1 – Introduction

MBDCA's are advanced algorithms that calculate dose with the consideration of material heterogeneities, where "model" refers to the modelling of the source and patient/treatment. Despite EBRT treatment planning utilizing algorithms that consider heterogeneities, TPSs in BT have only recently incorporated MBDCAs into their software. There are two MBDCAs that are now available clinically for HDR Ir-192 BT: the Advanced Collapsed-cone Engine (ACE) in Oncentra® Brachy (Elekta, Stockholm, Sweden), and the grid-based Boltzmann solver (GBBS) Acuros™ in BrachyVision (Varian, Palo Alto, CA) (13,14).

Many researchers have contributed to the development of the collapsed-cone superposition convolution (CCSC) algorithm, which is used within ACE to calculate the dose from scattered photons, however three seminal papers by Anhesjo and Carlsson Tedgren developed its application

to brachytherapy (15–17). Details on how ACE calculates dose are discussed in section 2.2. Acuros is a radiation therapy specific version of the GBBS Attila (Los Alamos National Laboratory, Los Alamos, NM), which is a deterministic solver that uses discrete ordinates (14,18,19). To determine the dose from scattered photons, the GBBS solves the linear Boltzmann transport equation by discretizing spatial, angular, and energy variables. This results in a system of linear equations that can be solved iteratively (20).

1.3.1.2 – Commissioning

The American Association of Physicists in Medicine (AAPM) Task Group 186 (TG-186) published a comprehensive guide to the types of MBDCAs that are being developed for brachytherapy, as well as recommendations on their commissioning for clinical use (21). Two levels of commissioning were recommended as a minimum. First, the TPS should be used to compare the dose distribution of a single source in a homogeneous water phantom, calculated by the MBDCA, to the dose distribution calculated with the traditional TG-43 formalism. The second level of commissioning investigates the effect of heterogeneities and various scatter conditions. Second level commissioning includes comparisons between 3D dose distributions as calculated with the TPS using the MBDCA, and bench-mark Monte Carlo (MC) simulations. The dose should be calculated for clinically relevant virtual phantoms, which implies that they represent the anatomy of patients.

Level 1 and 2 commissioning of ACE in Elekta's Oncentra® Brachy was undertaken by Papagiannis *et al.* for an Ir-192 HDR source (22). Using Oncentra® Brachy v4.4, a single Ir-192 source was modeled in a 30 cm diameter homogeneous water phantom. The ACE calculations were found to agree with TG-43 within 2% up to 5 cm away from the source. This 5 cm distance is the practical limit of ACE calculation accuracy. Beyond 5 cm, discretization artifacts in ACE become clearly evident. Level 2 commissioning was performed using virtual phantoms that simulated breast and esophageal treatments. Multiple source positions were used for these calculations. The

ACE calculations agreed well with the MC simulations, except for locations near the source catheter and in bone.

Relatively more evaluations of the Acuros™ GBBS in BrachyVision have been performed. Mikell *et al*. investigated the effects of source drive cable length for a single Ir-192 HDR source in a homogeneous water phantom (19). Acuros™ simulates a cable length of 1 mm, whereas BrachyVision TG-43 data is based on a 15 cm cable length. There was up to 20% dose deviation between MC and TG-43 for cable lengths of 1, 2, and 3 mm, at the cable end of the source. Others have found dose differences between Acuros™ and TG-43 calculations to be within 2% for most points in heterogeneous phantoms (22,23). Differences greater than 3% were observed on the drive cable side of the source.

Papagiannis *et al.* also investigated the previously mentioned virtual esophageal and breast phantoms using Acuros™. Dose differences between Acuros™ and MC were found to be within 2% for the majority of points, and up to 6% for some areas (22). The larger dose differences were attributed to inadequate ray trace sampling at the edges of geometric structures, or areas of large inhomogeneity. The dose differences between MC or Acuros™ and TG-43 calculations were found to be up to 10% in the lung and 20% in the breast (24).

For level 2 commissioning, Petrokokkinos *et al.* compared MC, Acuros™, and TG-43 for multiple dwell positions of an Ir-192 source in a partially shielded vaginal applicator. Acuros™ and MC were found to be within 2% for most points, however they deviated by 10% in the penumbra of the shield (25). This is still a significant improvement on the 20-30% difference found between TG-43 calculations and MC.

1.4 – Thesis Outline

Brachytherapy has been shown to achieve excellent patient outcomes for certain types and stages of cancer. However, there is definitely room for improvement in the planning of these treatments, because the currently used TG-43 dose calculation formalism assumes a homogeneous

water geometry. MBDCAs, on the other hand, do consider heterogeneities and have recently become available for clinical use. The research presented in this thesis investigates the use of the Advanced-Collapsed-cone Engine MDBCA for two different clinical applications: (i) gynecological cancer treatments that utilize a MCVC applicator, and (ii) treatments of NMSCs of the scalp. Experimental measurements of dose were performed using radiochromic film, and compared to TG-43 and ACE calculated doses in clinically relevant phantoms. The hypothesis under investigation is that these evaluations will contribute to clarifying the appropriate application of ACE in the clinic.

In this thesis, Chapter 2 discusses the theory and formalism for TG-43 and ACE dose calculations. The procedure and methodology for triple channel radiochromic film dose measurement is also described. Chapter 3 contains the methodology and results from experiments and calculations involving the MCVC applicator. An assessment of the use of ACE for scalp BT treatments is contained in Chapter 4. Lastly, Chapter 5 summarizes the conclusions from this work and presents future research possibilities.

1.5 – References

1. Delaney G, Jacob S, Featherstone C, Barton M. The role of radiotherapy in cancer treatment: Estimating optimal utilization from a review of evidence-based clinical guidelines [Electronic Version]. Cancer. 2005;104(6):1129–37.
2. Basil H. Brachytherapy, Conquering cancer, The first 100 years. Springfield, VA: Best Cure Foundation, Brachytherapy Research & Educational Foundation; 2014. 1-160 p.
3. Han K, Milosevic M, Fyles A, Pintilie M, Viswanathan AN. Trends in the utilization of brachytherapy in cervical cancer in the United States[Electronic Version]. Int J Radiat Oncol Biol Phys. Elsevier Inc.; 2013;87(1):111–9.
4. Petereit DG, Frank SJ, Viswanathan AN, Erickson B, Eifel P, Nguyen PL, et al. Brachytherapy: Where has it gone [Electronic Version]? J Clin Oncol. 2015;33(9):980–2.
5. Rose JN, McLaughlin PY, Hanna TP, D'Souza D, Sur R, Falkson CB. Surface mold

brachytherapy for nonmelanoma skin cancer: Canadian patterns of practice [Electronic Version]. Pract Radiat Oncol. American Society for Radiation Oncology; 2014;4(6):398–403.

6. Hoskin P, Coyle C, editors. Radiotherapy in Practice: Brachytherapy. 2nd ed. New York: Oxford University Press; 2011.
7. ICRU 38. Dose and volume specification for reporting intracavitary therapy in gynecology. ICRU 38. Bethesda, MD; 1985.
8. Van Dyk J, editor. The modern technology of radiation oncology: a compendium for medical physicists and radiation oncologists. Madison, WI: Medical Physics Publishing; 1999.
9. Ye S-J, Brezovich IA, Shen S, Duan J, Popple RA, Pareek PN. Attenuation of intracavitary applicators in 192Ir-HDR brachytherapy [Electronic Version]. Med Phys. 2004;31(7):2097–106.
10. Rodríguez ML, deAlmeida CE. Absorbed dose calculations in a brachytherapy pelvic phantom using the Monte Carlo method [Electronic Version]. J Appl Clin Med Phys. 2002;3(4):285–92.
11. Meigooni A, Nath R. Tissue inhomogeneity correction for brachytherapy sources in a heterogeneous phantom with cylindrical symmetry [Electronic Version]. Med Phys. 1991;19(2):401–7.
12. Chandola RM, Tiwari S, Kowar MK, Choudhary V. Effect of inhomogeneities and source position on dose distribution of Nucletron high dose rate Ir-192 brachytherapy source by Monte Carlo simulation [Electronic Version]. J Cancer Res Ther. 2010;6(1):54–7.
13. van Veelen B, Ma Y, Beaulieu L. ACE: Advanced Collapsed cone Engine (White Paper). White Paper Elekta. 2014;1–16.
14. Varian Medical Systems. BrachyVision ™ Acuros ™ Advanced brachytherapy dose calculations (brochure). Palo Alto. 2009;
15. Carlsson Tedgren AK, Ahnesjö A. Accounting for high Z shields in brachytherapy using collapsed cone superposition for scatter dose calculation [Electronic Version]. Med Phys.

2003;30(8):2206–17.

16. Ahnesjö A. Collapsed cone convolution of radiant energy for photon dose calculation in heterogeneous media [Electronic Version]. Med Phys. 1989;16(4):577–92.
17. Carlsson AK, Ahnesjö A. The collapsed cone superposition algorithm applied to scatter dose calculations in brachytherapy [Electronic Version]. Med Phys. 2000;27(10):2320–32.
18. Vassiliev ON, Wareing TA, McGhee J, Failla G, Salehpour MR, Mourtada F. Validation of a new grid-based Boltzmann equation solver for dose calculation in radiotherapy with photon beams [Electronic Version]. Phys Med Biol. 2010;55(3):581–98.
19. Mikell JK, Mourtada F. Dosimetric impact of an 192Ir brachytherapy source cable length modeled using a grid-based Boltzmann transport equation solver [Electronic Version]. Med Phys. 2010;37(9):4733–43.
20. Lewis E, Miller W. Computational methods of neutron transport. New York, NY, Wiley; 1984.
21. Beaulieu L, Carlsson Tedgren A, Carrier J-F, Davis SD, Mourtada F, Rivard MJ, et al. Report of the Task Group 186 on model-based dose calculation methods in brachytherapy beyond the TG-43 formalism: Current status and recommendations for clinical implementation [Electronic Version]. Med Phys. 2012;39(10):6208.
22. Papagiannis P, Pantelis E, Karaiskos P. Current state of the art brachytherapy treatment planning dosimetry algorithms. Br J Radiol [Internet]. 2014;87(1041):20140163. Available from: http://www.birpublications.org/doi/abs/10.1259/bjr.20140163
23. Zourari K, Major T, Herein A, Peppa V, Polgár C, Papagiannis P. A retrospective dosimetric comparison of TG43 and a commercially available MBDCA for an APBI brachytherapy patient cohort. Phys Medica [Internet]. 2015;1–8. Available from: http://linkinghub.elsevier.com/retrieve/pii/S1120179715001209
24. Zourari K, Pantelis E, Moutsatsos A, Sakelliou L, Georgiou E, Karaiskos P, et al. Dosimetric accuracy of a deterministic radiation transport based 192Ir brachytherapy treatment

planning system. Part III [Electronic Version]. Comparison to Monte Carlo simulation in voxelized anatomical computational models. Med Phys. 2013;40(1):011712.

25. Petrokokkinos L, Zourari K, Pantelis E, Moutsatsos a, Karaiskos P, Sakelliou L, et al. Dosimetric accuracy of a deterministic radiation transport based 192Ir brachytherapy treatment planning system. Part II: Monte Carlo and experimental verification of a multiple source dwell position plan employing a shielded applicator [Electronic Version]. Med Phys. 2011;38(4):1981–92.

Chapter 2 – Brachytherapy Dose Calculation and Measurement

2.1 – Dose Calculation

2.1.1 – Introduction to Radiation Dosimetry and Iridium-192

Energy from photon radiation is transferred to a material via three main types of interaction events: the photoelectric effect, Compton scattering, and pair production (1). The probability of these events occurring is described by interaction cross sections, and is dependent on photon energy, atomic number of the material, and electron density of the material. The cross section σ_{int} is related to the linear attenuation coefficient μ of a material by Equation 2.1, where M is the molar mass of the material, N_A is Avogadro's number, and ρ is the mass density. The linear attenuation of a narrow beam of N photons over a distance x is given by Equation 2.2.

$$\sigma_{int} = {\mu M}/{N_A \rho} \tag{2.1}$$

$$dN = -\mu N dx \rightarrow N = N_{\circ} e^{-\mu x} \tag{2.2}$$

A simple monoenergetic photon beam is defined by its fluence Φ and energy E. Fluence is defined as the number of particles incident on the cross sectional area of a unit sphere (dN/dA). Energy is deposited within a material by the slowing down of electrons, set in motion by incident photons, via Coulomb interactions. From this information, one can calculate the collisional KERMA (Kinetic Energy Released per unit MAss, Equation 2.3), where μ_{en}/ρ (mass energy absorption coefficient) describes linear attenuation per unit mass by interaction events that only deposit energy locally.

$$K = \Phi E \frac{\mu_{en}}{\rho} \tag{2.3}$$

When a photon beam travels through media, it will set charged particles into motion along the beam. If the energy of the charged particles of each type entering a region is equal to that leaving the region, then charged particle equilibrium (CPE) is achieved, and dose (energy deposited per unit mass) can be taken as the collisional KERMA.

As previously described, the probability of specific interaction events occurring, and therefore the probability of radiation dose being deposited, is dependent on incident photon energy. The photon energies from radionuclides are determined from the nature of their decay. Ir has two stable isotopes: Ir-191 with 37.2% natural abundance, and Ir-193 with 63.7% natural abundance. Neutron activation of Ir-191 is used to create Ir-192 via an (n,γ) reaction. In an (n,γ) reaction, the parent nucleus undergoes neutron capture and forms the daughter nucleus, which is in an excited state and therefore de-excites to the ground state via the emission of a photon. The depletion activation model best describes the radioactivation kinematics for reactions involving a daughter being activated by radioactivation particles (2). The number of daughter nuclei (N_{Ir192}) is given by Equation 2.4, with the solution given by Equation 2.5. The solution assumes that initially $N_{Ir192}(t=0)$ is zero, and ignores granddaughter decay. σ_{Ir191} is the activation cross section of Ir-191, σ_{Ir192} is the activation cross section of Ir-192, λ_{Ir192} equals ln(2) divided by the Ir-192 half-life, and $\dot{\varphi}$ is the incident neutron fluence rate.

$$\frac{dN_{Ir192}}{dt} = \sigma_{Ir191}\dot{\varphi}N_{Ir191}(t) - \lambda_{Ir192}N_{Ir192}(t) - \sigma_{Ir192}\dot{\varphi}N_{Ir192}(t) \tag{2.4}$$

$$N_{Ir192}(t) = N_{Ir191}(0) \cdot \frac{\sigma_{Ir191}\dot{\varphi}}{\lambda_{Ir192}+\sigma_{Ir192}\dot{\varphi}-\sigma_{Ir191}\dot{\varphi}} \cdot \left(e^{-\sigma_{Ir191}\dot{\varphi}t} - e^{-(\lambda_{Ir192}+\sigma_{Ir192})\dot{\varphi}t}\right) \tag{2.5}$$

Ir-192 decays to Platinum-192 (Pt-192) and Osmium-192 (Os-192) by beta-minus decay and electron capture, respectively. The excited states of Pt-192 and Os-192 decay to their ground states by the emission of photons, which form the Ir-192 photon spectrum. The photon spectrum for Ir-192 decay is relatively complex, with 14 photon energies that yield an effective energy of 0.38 MeV. At this energy, Compton scattering, which is the inelastic scattering of the photon with an atomic electron, is dominant. The change in wavelength of a photon due to Compton scattering is given by Equation 2.6, where λ is the incoming photon wavelength, λ' is the scattered photon wavelength, c_{sp} is the speed of light, m_e is the electron rest mass, h is Planck's constant, and θ_{defl} is the angle of deflection of the photon. The probability of Compton scattering increases with

increasing electron density and is negligibly dependent on the atomic number of the scattering material (1).

$$\lambda' - \lambda = \frac{h}{m_e c_{sp}}(1 - cos\ \theta_{\text{defl}}) \tag{2.6}$$

2.1.2 – TG-43 Dose Calculation Formalism

2.1.2.1 – Basic Formalism

Current clinical practice in brachytherapy treatment planning uses the American Association of Physicists in Medicine (AAPM) TG-43 protocol (3,4). Originally published in 1995, TG-43 has since been updated to consider new sources and improved dosimetric characterization of certain sources. This section will describe the formalism outlined in the TG-43 documents. Figure 2.1 illustrates the coordinate system used in this formalism.

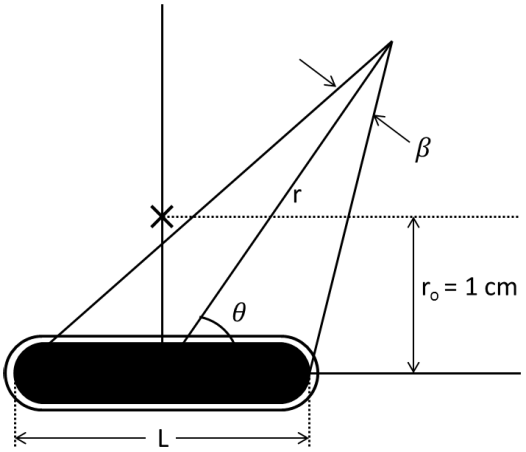

Figure 2.1 – Illustration of geometry for TG-43 formalism.

Multiplicative dose factors are pre-determined by measurement or Monte Carlo simulation of the BT source dose distribution in water. TPSs then incorporate these dose factors into look-up tables, such that the dose at any point around a given source can be determined in the software. Equation 2.7 gives the dose rate at a distance r and polar angle θ from a cylindrically symmetric source. Air kerma strength (S_k) is defined as the air kerma rate ($\dot{K}_\delta$) due to photons with energies greater than δ at a specific distance (d), along the transverse axis of the source, multiplied by the

distance squared. The distance is usually on the order of 1 m, and $\dot{K}_\delta$ is measured with a spherical cavity chamber or wide-angle-free-air-chamber (WAFAC) for HDR and LDR sources, respectively (5). One unit of S_k (1 U) is defined as 1 centi-Gray (cGy) centimeter squared per hour.

$$\dot{D}(r,\theta) = S_k \cdot \Lambda \cdot \frac{G(r,\theta)}{G(r_o,\theta_o)} \cdot g(r) \cdot F(r,\theta) \tag{2.7}$$

$$S_k = \dot{K}_\delta(d) d^2 \tag{2.8}$$

The dose rate constant (Λ), geometry function ($G(r,\theta)$), radial dose function ($g(r)$), and anisotropy function ($F(r,\theta)$), are determined by measurement or Monte Carlo simulations for each BT source. Λ allows for conversion of $\dot{K}_\delta$ to the dose rate to water at 1 cm (r_o) on the transverse axis of the source (θ_o = 90°). Λ considers the spatial distribution of radioactivity within the source, encapsulation and filtration due to the source materials, and scattering within the water medium. $G(r,\theta)$ accounts solely for axial and polar dose variations due to the spatial distribution of radioactivity in the source. Sources are commonly approximated by a line, such that $G(r,\theta)$ is given by Equation 2.10. Factors $g(r)$ and $F(r,\theta)$ account for photon attenuation and scatter at locations in the transverse plane and out of the transverse plane, respectively. The TG-43 data used in this thesis is the consensus data from the High Energy Brachytherapy Source Dosimetry Working Group (6).

$$\Lambda = \frac{\dot{D}(r_o,\theta_o)}{S_k} \tag{2.9}$$

$$G_L = \begin{cases} \frac{\beta}{Lr\sin\theta} & \text{if } \theta \neq 0° \\ (r^2 - L^2/4)^{-1} & \text{if } \theta = 0° \end{cases} \tag{2.10}$$

$$g(r) = \frac{\dot{D}(r,\theta_o)}{\dot{D}(r_o,\theta_o)} \frac{G(r_o,\theta_o)}{G(r,\theta_o)} \tag{2.11}$$

$$F(r,\theta) = \frac{\dot{D}(r,\theta)}{\dot{D}(r,\theta_o)} \frac{G(r,\theta_o)}{G(r,\theta)} \tag{2.12}$$

2.1.2.2 – The microSelectron HDR source

As previously noted, TG-43 parameters are dependent on the design of the source and properties of the radionuclide. This section will describe the properties of three different microSelectron HDR source models, and discuss the effects the designs have on the TG-43 parameters.

The microSelectron HDR source is composed of a solid iridium core, surrounded by a stainless steel capsule. There have been three different versions of this source, which will be referred to as the 1995 (7), 1998 (8), and 2010 (9) models. These models are illustrated in Figure 2.2.

The original 1995 Ir-192 core was a cylinder with a 0.6 mm diameter and 3.5 mm active length. The cylindrical shape lends to relatively heavy filtration through the long axis of the cylinder due to the high density of the core. The filtration and line source geometry are the dominant causes for the observed 20-30% dose reduction at the source tip and drive cable ends. Figure 2.3 illustrates this anisotropy for the 2010 model, which is evident by the distinctive "pinching" of the isodose lines at the tip and tail of the source.

There are two key differences between the 1995 and 1998 source models: (i) the drive cable of the 1998 model is narrower, and (ii) the Ir-192 core of the 1998 model has beveled edges, while the 1995 model does not. The thinner drive cable of the 1998 source is the main cause of the maximum 5% dose difference observed relative to the 1995 source, and is manifest in the $F(r,\theta)$ values at the drive cable end. Additionally, the beveled edges of the core allow for a thinner stainless steel capsule at the source tip. The result of these modifications was an up to 8% difference in $F(r,\theta)$ from the 1995 model. However, this difference occurred at very small distances from the source ($r<2.5$ mm), which would only be clinically relevant for interstitial treatments and not for treatments using intracavitary applicators. The beveled edges of the 1998 model resulted in the line source geometry not being as accurate as for the 1995 model. Only very minor changes were made to the 2010 source model, and $F(r,\theta)$ was within 2% of the 1998 model for $r>2.5$ mm.

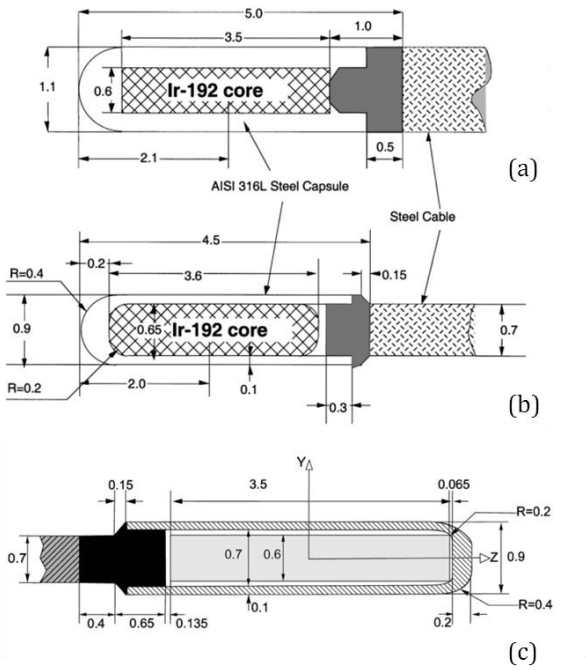

Figure 2.2 – Schematic diagrams of the 1995 (a), 1998 (b), and 2010 (c) versions of the microSelectron HDR source (8,9). Dimensions are in millimeters. [Reprinted with permission from: (a, b) Daskalov GM, Loffler E, Williamson JF. Monte Carlo-aided dosimetry of a new high dose-rate brachytherapy source [Electronic Version]. Med Phys. 1998;25(11):2200–8. And (c) Granero D, Vijande J, Ballester F, Rivard MJ. Dosimetry revisited for the HDR 192Ir brachytherapy source model mHDR-v2 [Electronic Version]. Med Phys. 2011;38(1):487–94. See Appendix for documentation].

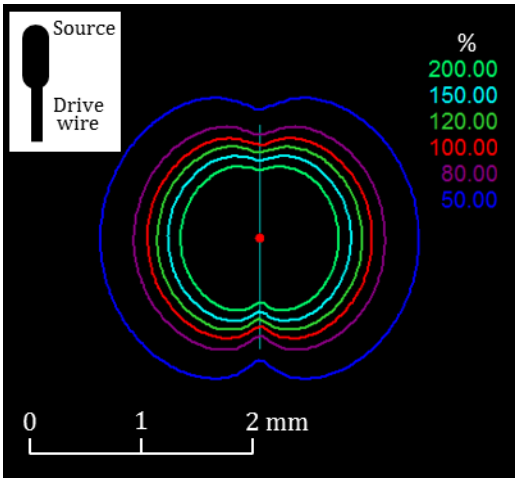

Figure 2.3 – Isodose distribution in the source longitudinal plane for a single Ir-192 source (2010 model) as computed using TG-43 in Oncentra Brachy v4.5. The source orientation is specified in the inset.

2.1.3 – The Advanced Collapsed-cone Engine

2.1.3.1 – Dose Calculation Approach

Details of how ACE calculates dose are reported in a white paper from Elekta (10). In the white paper, the term "voxel" is used to describe a cubic element in the calculation grid. In this thesis, the following terms will be used: (i) "grid size" will refer to the calculation grid resolution (isotropic), and (ii) "grid element" will refer to a single cubic element in the calculation grid. Any use of the term "voxel" will be reserved for cubic volumes in which doses calculated by ACE have been averaged.

ACE calculates dose as the sum of the contributions from the primary photons, once scattered photons, and any residual scatterings. The primary dose is calculated using a ray trace algorithm. In the ray trace algorithm, the fluence is attenuated along a rayline to the grid element where the dose is calculated. Equation 2.13 gives the primary KERMA, per unit of radiant energy emitted from the source, to a grid element at $\vec{x}$. This equation expresses exponential attenuation of the fluence, through a distance Δr_i in each grid element i, using the linear attenuation coefficient for

that grid element (μ_i) averaged over the photon spectrum (Figure 2.4). In Equation 2.13, γ_c accounts for the average IS to a grid element, v is the volume of the grid element, θ is the angle between the direction of the source alignment and vector from the source to the grid element, $\Psi(\theta)$ is a correction factor for scattering and absorption anisotropy of the source, and $\bar{\mu}_{en}(\vec{x})$ is the spectrally averaged mass energy absorption coefficient for the grid element. CPE is assumed and dose is equated to KERMA. The assumption of CPE is accurate for particle energies used in brachytherapy because the photon mean free path is significantly larger than the ranges of secondary electrons (11).

$$\frac{K_{prim}(\vec{x})}{R} = \gamma_c(r,\theta,v)\frac{\Psi(\theta)}{4\pi r^2}\cdot\left.\frac{\bar{\mu}_{en}(\vec{x})}{\rho}\right|_{med}\cdot e^{-m(\theta)\sum_{i\in rayline\ to\ x}(\bar{\mu}/\rho)_i\cdot\rho_i\cdot\Delta r_i} \tag{2.13}$$

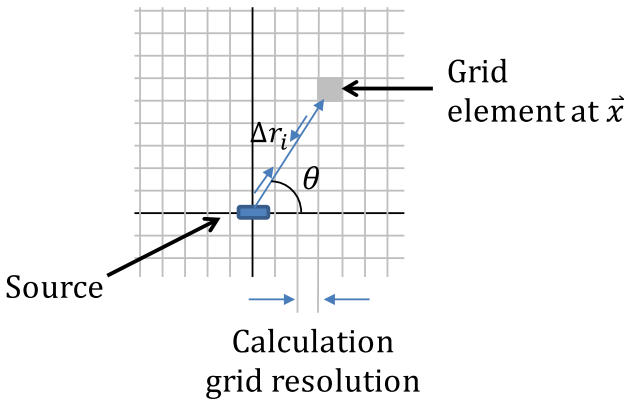

Figure 2.4 – 2D illustration of the calculation grid for ACE algorithm.

The energy scattered in grid element $\vec{x}$, or SCERMA, is then determined by multiplying the primary KERMA (Equation 2.13) with the ratio of spectrally averaged linear attenuation ($\bar{\mu}$) to mass energy absorption coefficients ($\bar{\mu}_{en}$, Equation 2.14). The SCERMA is then input into the collapsed-cone superposition convolution (CCSC) algorithm. CCSC determines the scatter dose to a grid element at $\vec{x}$ by convolving the first scattered SCERMA with a pre-calculated dose kernel (h), which has been

discretized into cones that point in particular radiation transport directions (Equation 2.15). B_θ and b_θ are parameters used for fitting MC derived kernel data. The energy within a cone is collapsed such that the inverse square (IS) of the kernel is removed and the energy is transported only along the central axis of the cone (Equation 2.16). The transport directions are a uniform spherical tessellation around each scattering center.

$$\frac{S_{1sc}(\vec{x})}{R} = \frac{(\bar{\mu}(\vec{x})/\rho)_{med} - (\bar{\mu}_{en}(\vec{x})/\rho)_{med}}{(\bar{\mu}_{en}(\vec{x})/\rho)_{med}} \cdot \frac{K_{prim}(\vec{x})}{R} \tag{2.14}$$

$$\frac{D_{1sc}(\vec{x})}{R} = \iiint_V \frac{S_{1sc}(\vec{x}')}{R} \tilde{h}_s(|\vec{x} - \vec{x}'|, \theta) d^3\vec{x}' \tag{2.15}$$

$$\tilde{h}_s = B_\theta \, e^{-b_\theta|\vec{x}'-\vec{x}|}/|\vec{x}' - \vec{x}|^2 \rightarrow B_\theta e^{-b_\theta|\vec{x}'-\vec{x}|} \tag{2.16}$$

For brachytherapy, the first scattered SCERMA (S_{1sc}) deposited in a grid element is then used to calculate the second scattered SCERMA (S_{2sc}), which is used to determine the dose from residual scatterings. Further details are given in Section 2.1.3.2.

The number of scatter transport directions is dependent on whether the high accuracy (hACE) or standard accuracy (sACE) mode of ACE is used. For a single dwell position, hACE calculates the scatter dose using 1620/320 first/residual scatter transport directions, and sACE uses 320/180 first/residual scatter transport directions. The number of transport directions decreases as the number of dwell positions increases. To speed up the calculations, multiple calculation grid sizes are used. The grid size used in ACE calculations depends on the distance from each dwell position. To determine the grid size, ACE first defines a box that contains all the dwell positions. A margin is then added to that box, which will contain a particular grid size. For example, hACE has a 1 mm grid size up to 80 mm from a dwell position in the x, y, and z directions, when more than one dwell position is used. Table 2.1 gives the margins and corresponding grid sizes for the high and standard accuracy ACE calculations when 2 to 50 dwell positions are used.

Table 2.1 – Calculation grid resolutions for the high and standard accuracy ACE calculations when the number of dwell positions is between 2 and 50.

Margin (mm)	High Accuracy Grid Size (mm)	Standard Accuracy Grid Size (mm)
10	N/A	1
80	1	2
200	2	5

2.1.3.2 – Application to Brachytherapy

The scatter dose component is relatively high for brachytherapy, therefore the accuracy of the dose calculation is dependent on the accuracy of the scatter dose calculation. ACE addresses this issue by separately modelling multiple scattering events, as previously mentioned. Figure 2.5, from Carlsson *et al*. (11), plots the dose in water per primary photon radiant energy as a function of distance *r* from a uniform spherical source, for photons at 350 keV. The scatter dose is observed to exceed the primary dose at just over 5 cm from the source. To calculate the dose from secondary scattering events, the first scatter dose D_{1sc} deposited in the grid element located at $\vec{x}$ is multiplied by the ratio of spectrally averaged linear energy absorption ($\bar{\mu}_{en,1sc}$) and linear attenuation coefficients (Equation 2.17). The second scattered SCERMA is then convolved with the pre-determined multi-scatter point kernel $\widetilde{H}_{msc}$. The isotropic version of this convolution is given in Equation 2.18. For brachytherapy, bi-exponential functions are used to accurately describe the kernels, and the kernels must be tilted with respect to the diverging primary fluence ray.

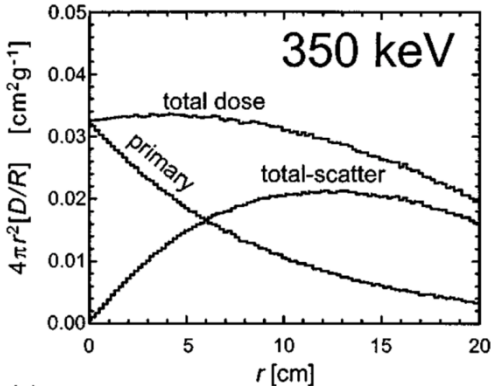

Figure 2.5 – Primary and scatter dose contributions in water medium for photons at 350 keV. The dose distributions were determined by Carlsson *et al.* (11), using Monte Carlo simulation, and are multiplied by the distance squared and normalized to the primary photon energy. [Reprinted with permission from: Carlsson AK, Ahnesjö A. The collapsed cone superposition algorithm applied to scatter dose calculations in brachytherapy [Electronic Version]. Med Phys. 2000;27(10):2320–32. See Appendix for documentation.]

$$S_{2sc}(\vec{x}) = \frac{1-\overline{\mu}_{en,1sc}/\overline{\mu}_{1sc}}{\overline{\mu}_{en,1sc}/\overline{\mu}_{1sc}} \cdot D_{1sc}(\vec{x}) \tag{2.17}$$

$$D_{msc}(\vec{x}) = \iiint_V \frac{S_{2sc}(\vec{x})}{R} \widetilde{H}_{msc}(\vec{x}-\vec{x}')d^3\vec{x}' \tag{2.18}$$

The collapsed-cone approximation is exact close to a scattering event, where the grid size is larger than the conical cross sectional area. However, farther from the scattering center the conical area will be larger than the grid size resulting in too much energy being deposited on the cone central axis, and too little off the central axis. This produces the "ray effect" as illustrated in Figure 2.6. The errors associated with the approximation are particularly critical for brachytherapy due to the steep fluence gradient resulting in neighboring grid elements having very different SCERMA values. By contrast, in EBRT the SCERMA values are similar and therefore discretization errors wash out (11). Both an increase in the number of scatter transport directions and an increase in calculation grid size mitigate this error by decreasing the number of grid units within a transport cone.

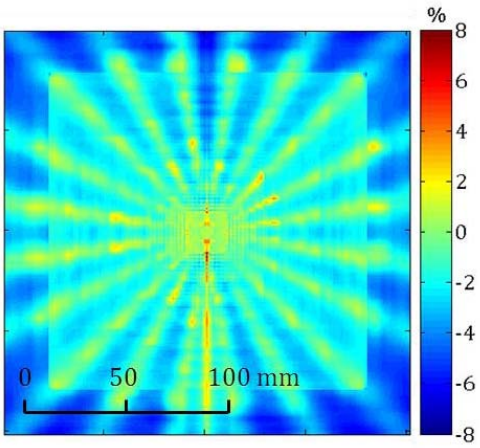

Figure 2.6 – Percent dose difference between the standard accuracy ACE calculation and TG-43 calculation for an Ir-192 source in water. This figure clearly illustrates the ray effect caused by the CCSC approximation.

2.1.3.3 – Calculations in High Atomic Number Materials

The photon scatter spectrum in high atomic number (Z) materials can be significantly different from that of water. Therefore, Carlsson-Tedgren and Ahnesjö have derived scaling factors for the pre-determined scatter kernels (12). Equation 2.19 shows the derived scaling factors applied to the first scatter kernel ($\tilde{h}_{1sc}$); η_{1sc} is used when the scatter energy is released locally into the heterogeneous medium (Equation 2.20), and $\tilde{\eta}_{1sc}$ is used when energy is deposited upstream of a heterogeneity (Equation 2.21). χ_{1sc} scales the fraction of first scattered energy that is absorbed (Equation 2.22). The energy spectrum variables $\Psi_{1sc-med}$ and Ψ_{1sc-w} denote that the coefficients are being averaged over the photon spectra in medium (*med*) and water (*w*), respectively.

$$\tilde{h}_{1sc}(r,\theta) = \chi_{1sc}\frac{B_\theta}{b_\theta}e^{-b_\theta\tilde{\eta}_{1sc}r}/r^2 \tag{2.19}$$

$$\eta_{1sc} = (\bar{\mu}_{1sc})_{med,\Psi_{1sc-med}}/(\bar{\mu}_{1sc})_{w,\Psi_{1sc-w}} \tag{2.20}$$

$$\tilde{\eta}_{1sc} = (\bar{\mu}_{1sc})_{med,\Psi_{1sc-w}}/(\bar{\mu}_{1sc})_{w,\Psi_{1sc-w}} \tag{2.21}$$

$$\chi_{1sc} = \frac{(\bar{\mu}_{en,1sc}/\bar{\mu}_{1sc})_{med,\Psi_{1sc-med}}}{(\bar{\mu}_{en,1sc}/\bar{\mu}_{1sc})_{w,\Psi_{1sc-w}}} \tag{2.22}$$

2.1.4 – Uncertainty Calculations

The uncertainty analysis for TG-43 and ACE calculated doses used in this thesis will now be described. For a single dose point calculated by TG-43 in OcB, the combined type B uncertainty is obtained from the combination of uncertainties from the air kerma strength (S_k), the reference Monte Carlo dose estimate, and the treatment planning system interpolation (Equation 2.23). The values used here are from DeWerd *et al.* for high energy BT sources (13). The type B uncertainty associated with ACE calculated doses was estimated from analyses by others to be 5% (14,15). The type A uncertainty associated with the average dose taken from N dose points with the standard deviation $\sigma_{D,calc}$, is given by Equation 2.24. When average doses ($\overline{D}$) were calculated from TG-43 or ACE data, the associated type A uncertainty was added in quadrature with the 3.4% or 5% type B uncertainty, respectively (Equation 2.25).

$$\sigma_{B,calc} = \sqrt{{\sigma_{S_k}}^2 + {\sigma_{MC}}^2 + {\sigma_{TPS}}^2} = \sqrt{1.5^2 + 1.6^2 + 2.6^2} = 3.4\% \tag{2.23}$$

$$\sigma_{A,calc} = \frac{\sigma_{D,calc}}{\sqrt{N}} \tag{2.24}$$

$$\sigma_{\overline{D},calc} = \sqrt{{\sigma_{B,calc}}^2 + {\sigma_{A,calc}}^2} \tag{2.25}$$

If σ_{abs} denotes an absolute uncertainty and σ_{rel} denotes a relative uncertainty, then the percent dose difference between TG-43 and ACE calculated doses was calculated by:

$$\Delta D(\%) = 100 * \frac{(\overline{D}_{ACE} \pm \sigma_{abs,ACE}) - (\overline{D}_{TG43} \pm \sigma_{abs,TG43})}{(\overline{D}_{TG43} \pm \sigma_{abs,TG43})} = \frac{100 * (\overline{D}_{ACE} - \overline{D}_{TG43}) \pm \sqrt{{\sigma_{abs,ACE}}^2 + {\sigma_{abs,TG43}}^2}}{(\overline{D}_{TG43} \pm \sigma_{abs,TG43})}$$

$$= \frac{100 * (\overline{D}_{ACE} - \overline{D}_{TG43}) \pm \sigma_{abs,diff}}{(\overline{D}_{TG43} \pm \sigma_{abs,TG43})} = \frac{100 * (\overline{D}_{ACE} - \overline{D}_{TG43})}{\overline{D}_{TG43}} \pm \sqrt{{\sigma_{rel,diff}}^2 + {\sigma_{rel,TG43}}^2}$$

$$= \Delta D\ (\%) \pm \sigma_{rel,\Delta D}(\%\ of\ \%) = \Delta D\ (\%) \pm \sigma_{abs,\Delta D}(\%\ )$$

2.2 – Dose Measurement

2.2.1 – Introduction

The importance of experimental verification of MBDCAs for clinically relevant phantoms was stressed by the report of the AAPM Task Group 186 (16). Researchers have presented results based on a range of dosimetric methodologies including ion chambers (17), thermoluminescent dosimeters (17), optically stimulated luminescent dosimeters (18), 3D polymer gel dosimeters (19), and radiochromic film (17). Radiochromic film is distinguished by its high spatial resolution, weak energy dependence (20–22), and near tissue equivalence (23). However, using it to make accurate dose measurements is not trivial; therefore a detailed description of how it was used for work in this thesis is given.

2.2.2 - Radiochromic Film Dosimetry

2.2.2.1 – Gafchromic EBT3 Film

Gafchromic EBT3 film consists of a 28 μm thick active layer of lithium pentacosa-10,12-dyinoic acid, surrounded on both sides by matte polyester layers for a total thickness of 0.27 mm (24) (Figure 2.7). The matte polyester substrate is a change from the original polyester of EBT and EBT2 films, which caused Newton's rings formation during scanning. Newton's rings are the constructive and destructive interference of light created when the distance between the polyester layer and the glass of the scanner is on the order of a wavelength. The new matte polyester is treated with silica particles to prevent this (25).

When ionizing radiation impinges on the film, the crystals in the active layer form coloured polymers that increase in length with increasing radiation fluence; therefore, the optical density of the film increases with increasing dose. A calibration curve relating the optical density to dose for each of three different colour channels (red-green-blue in a colour scanner) is obtained and used to determine the dose for an unknown irradiation.

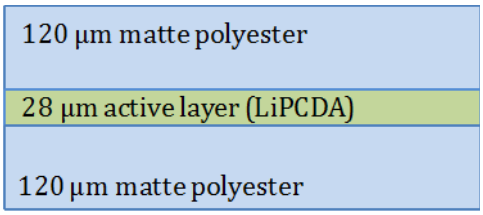

Figure 2.7 – Illustration of Gafchromic EBT3 film layers.

2.2.2.2 – Calibration Curve Fitting

The use of radiochromic film to measure absolute doses requires determining a set of calibration curves that relate dose to optical density. The procedure used for this thesis work will now be described. Gafchromic EBT3 film has been shown to be energy independent for photons with energies greater than 50 keV. This allows for a 6 MV photon beam from a linac to be used to determine the calibration curve for Ir-192. Pieces of film are irradiated at 13 dose levels between 0 Gy and 10 Gy. The film is irradiated with a 10x10 cm^2 field at the depth of maximum dose (1.5 cm) in solid water, with 12 cm of solid water placed below the film for backscatter. The daily linac output is measured before and after film irradiations with an ion chamber (Capintec PR-06, Ramsey, NJ), and the intended dose levels are corrected with a multiplicative factor equal to the measured output divided by the expected output. The calibration films are then scanned with an Epson Expression 10000 XL scanner (Seiko Epson Corp., Nagano, Japan). This scanner has a xenon fluorescent lamp, and an alternating six-line CCD detector. The films are scanned at 72 dpi, 48-bit RBG colour (16-bits per colour channel), and the scans are saved as tagged image file format images. The average pixel value (PV) in a region of interest at the center of the film piece is determined for each colour channel and each film piece (dose level), and normalized to the maximum PV for a 16 bit integer (2^{16} - 1 = 65535)

The vendor recommends that the normalized film response *X(D)* be described with a linear rational function (Equation 2.26) because the function's behavior is qualitatively similar to film (25). In Equation 2.26, *a*, *b*, and *c* are the calibration curve fitting parameters, and *D* is the dose.

Optical density (OD) is the base 10 logarithm of the ratio of the transmitted light intensity to incident light intensity, and therefore is given by Equation 2.27.

$$X(D) = \frac{a+bD}{c+D} \tag{2.26}$$

$$\text{OD} = -log_{10}\left(\frac{a+bD}{c+D}\right) \tag{2.27}$$

Ramos *et al* (26) describe several methods for determining the calibration curve fitting parameters; the direct optimization approach with an effective variance (EV_{opt}) is described here. The non-linear least squares method is used to minimize the difference between the measured optical density (y_i) and the optical density calculated from the linear rational function $f(c_j, x_i)$. In Equation 2.28, c_j is a fitting parameter ($j=1,2,3=a,b,c$ from Equation 2.27) and x_i is the reference dose ($i=1:13$ for 13 dose levels). An effective variance ($\sigma_{y,i,eff}$, Equation 2.29) is used to include uncertainties in the linac reference doses ($\sigma_{x,i}$).

$$\arg\min \sum_{i=1}^{n} \left[\frac{y_i - f(c_j, x_i)}{\sigma_{y,i,eff}}\right]^2 \tag{2.28}$$

$${\sigma_{y,i,eff}}^2 = {\sigma_{y,i}}^2 + \left(\frac{\partial f(c_j, x_i)}{\partial x}\right)^2 {\sigma_{x,i}}^2 \tag{2.29}$$

2.2.2.3 – Triple Channel Film Dosimetry

Gafchromic EBT film was originally intended for use with red and blue color channels. The red color channel has the greatest sensitivity to lower doses, and its response to irradiation predominantly contains information about dose. The blue color channel allows for extension of the dynamic range to higher doses, and is dominated by information about film uniformity. A yellow marker dye was added to EBT2 and EBT3 Gafchromic films, which is not affected by radiation. The addition of the marker dye allows for three color channels (red, green, and blue) to be used. Triple channel analysis is a method that uses all three channels to remove effects resulting from non-dose dependent components of the film, such as variation in active layer thickness, scratches, or

fingerprints. The methodology has been described in detail by Micke *et al* (27), and will be summarized here.

A disturbance parameter Δd is included in the calculation of the dose. If τ is the film thickness, $\bar{\tau}$ is the mean film thickness, and $f_k(D)$ is the linear rational function, then the optical density for colour channel k (OD_k) is given by Equation 2.30, and the dose measured by color channel k (D_k) is given by Equation 2.31. Due to the calibration curve of each color channel being unique, a given disturbance parameter Δd will not result in the same change in dose. Therefore, Δd is found by minimizing the sum of the squared differences in dose between each pair of colour channels by setting the first derivative of Ω to zero (Equations 2.32 and 2.33).

$$\mathrm{OD}_k(D) = f_k(D) \cdot \tau/\bar{\tau} \tag{2.30}$$

$$D_k = f_k^{-1}\left(\mathrm{OD}_k \cdot \Delta d\right) = \frac{c_k \cdot 10^{-\mathrm{OD}_k \cdot \Delta d} - a_k}{b_k - 10^{-\mathrm{OD}_k \cdot \Delta d}} \tag{2.31}$$

$$\Omega(\Delta d) = \sum_{i \neq j} \left(D_{k_i} - D_{k_j}\right)^2 \tag{2.32}$$

$$\frac{d}{d\Delta d}\Omega = 0 \tag{2.33}$$

After a piece of film with an unknown dose is scanned, Δd is solved for in Matlab (Mathworks, Natick, MA) for each pixel using Newton's method. Newton's method iteratively solves for Δd by repeatedly applying Equation 2.34 until a solution is found within a desired threshold (28).

$$\Delta d_{n+1} = \Delta d_n - \frac{\Omega'(\Delta d_n)}{\Omega''(\Delta d_n)} \tag{2.34}$$

2.2.2.4 – Uncertainty Calculations

Uncertainty calculations pertaining to the radiochromic film measurements follow the principles outlined in the NIST Technical Note 1297 (29), and implemented by Morrison *et al* (30) and Chiu-Tsao *et al* (31). Both type A and type B uncertainty components will be described here. An uncertainty component in the type A category is represented by a statistical estimate of the

standard deviation of a series of observations. Evaluation of uncertainty by means other than a statistical analysis of a series of observations is considered a type B uncertainty. Type B uncertainties may be considered to approximate a standard deviation. They may be estimated from previous measurement data, uncertainties assigned to reference data, or upper and lower limits.

The uncertainty associated with the use of the derived calibration curve to determine a measured dose arises from three sources: the measured optical density, the calibration curve fitting parameters, and the reference linac doses. By standard propagation of error (Equation 2.35), the uncertainty for a single dose measurement using a single color channel is given by Equation 2.36, where D_{film} is the dose to film.

$$\sigma_y{}^2 = \sum_i \left(\frac{\partial y}{\partial x_i}\right)^2 \cdot \sigma_{x_i}{}^2 \tag{2.35}$$

$$\sigma_{Dfilm}(\%) = \frac{\sqrt{\left(\frac{\partial D_{film}}{\partial \mathrm{OD}}\right)^2 \sigma_{\mathrm{OD}}{}^2 + \left(\frac{\partial D_{film}}{\partial a}\right)^2 \sigma_a{}^2 + \left(\frac{\partial D_{film}}{\partial b}\right)^2 \sigma_b{}^2 + \left(\frac{\partial D_{film}}{\partial c}\right)^2 \sigma_c{}^2 + \left(\frac{\partial D_{film}}{\partial D_{ref}}\right)^2 \sigma_{Dref}{}^2}}{D_{film}} \times 100 \tag{2.36}$$

Uncertainty in dose arising from uncertainty in optical density of the calibration curve is obtained from differentiation of the inverse of Equation 2.27 and is given by Equations 2.37 and 2.38.

$$\frac{\partial D_{film}}{\partial \mathrm{OD}} = \frac{\ln(10)10^{\mathrm{OD}}(a - b \cdot c)}{(b \cdot 10^{\mathrm{OD}} - 1)^2} \tag{2.37}$$

$$\sigma_{\mathrm{OD}}(\%) = \frac{1}{\ln(10)} \sqrt{\left(\frac{\sigma_{PV}}{PV}\right)^2 + \left(\frac{\sigma_{PVblank}}{PV_{blank}}\right)^2} \tag{2.38}$$

Each calibration film is scanned three times such that:

$$\sigma_{PV} = \frac{1}{3}\sqrt{\sigma_{PV1}{}^2 + \sigma_{PV2}{}^2 + \sigma_{PV3}{}^2} \tag{2.39}$$

Uncertainty in estimated dose due to each of the calibration curve parameters is given by Equations 2.40 through 2.42. $\sigma_a, \sigma_b,$ and σ_c are estimated by finding the values that minimize the difference between the measured and fit doses. The uncertainty in the linac output (σ_{Dref}) is taken to be 1%.

$$\frac{\partial D_{film}}{\partial a} = \frac{10^{\mathrm{OD}}}{1 - b \cdot 10^{\mathrm{OD}}} \tag{2.40}$$

$$\frac{\partial D_{film}}{\partial b} = \frac{10^{\mathrm{OD}}(a \cdot 10^{\mathrm{OD}} - c)}{\left(b \cdot 10^{\mathrm{OD}} - 1\right)^2} \tag{2.41}$$

$$\frac{\partial D_{film}}{\partial c} = \frac{1}{b \cdot 10^{\mathrm{OD}} - 1} \tag{2.42}$$

When triple channel analysis is used, the final dose is taken as a weighted mean with respect to the uncertainties associated with each color channel. The propagation of calibration curve uncertainty through this weighting will now be described. Let $\sigma_i(D)$ be the uncertainty in dose D for colour channel *i,* where *i* can be the red, green, or blue colour channel. Let *k* denote a specific colour channel. The weight *w* for a dose *D*, determined from the calibration curve of channel *k* and triple channel analysis, is given by:

$$w_k(D) = \left(\frac{\sum_{i=1}^{3} \sigma_i(D)}{\sigma_k(D)}\right)^{-2} \tag{2.43}$$

The weighted dose is then:

$$D_w = \frac{\sum_{i=1}^{3} D_i w_i(D)^{-2}}{\sum_{i=1}^{3} w_i(D)^{-2}} \tag{2.44}$$

The uncertainty of the weighted dose is given by:

$$\sigma_{D_w}(D) = \frac{1}{\sum_{i=1}^{3} w_i(D)^{-2}} \cdot \left(\sum_{i=1}^{3} w_i(D)^{-4} \sigma_i(D)^2 {D_i}^2\right)^{1/2} \tag{2.45}$$

The uncertainty arising from the use of triple channel analysis is taken as the average value of the absolute differences between the doses determined from each calibration curve:

$$\sigma_{TC} = \frac{1}{3D_w} \sum_{\substack{i,j=1 \\ i \neq j}}^{3} \left|D_i - D_j\right| \tag{2.46}$$

The total uncertainty for the weighted dose determined from the calibration curves and triple channel analysis is the quadrature sum of the triple channel uncertainty and weighted dose uncertainty. The total uncertainty for a single film pixel will henceforth be referred to as the type B film uncertainty:

$$\sigma_{B,\mathrm{film}} = \sqrt{{\sigma_{TC}}^2 + {\sigma_{D_w}}^2} \tag{2.47}$$

When an average value of dose is obtained from N pixels that have a standard deviation $\sigma_{\bar{D}}$, the associated type A uncertainty is:

$$\sigma_{A,\text{film}} = \frac{\sigma_{\bar{D}}}{\sqrt{N}} \tag{2.48}$$

Finally, the total uncertainty for an average film dose $\bar{D}$ determined from N pixels is the quadrature sum of the type A and type B uncertainties:

$$\sigma_{\bar{D},\text{film}} = \sqrt{\sigma_{B,\text{film}}(\bar{D})^2 + {\sigma_{A,\text{film}}}^2} \tag{2.49}$$

For the calculation of percent dose differences between film measured doses and TG-43 or ACE calculated doses, uncertainties are propagated as described in Section 2.1.4. All results are stated with expanded uncertainties, such that total uncertainties (σ_{total}) are multiplied by a coverage factor of 2 (k=2). For a quantity X (estimated by the measured value x), a coverage factor of 2 specifies the 95% confidence interval of X: $x - k\sigma_{total} \leq X \leq x + k\sigma_{total}$, which is written as $x \pm k\sigma_{total}$ (29).

2.3 – References

1. Johns HE, Cunningham JR. The physics of radiology. 4th ed. Springfield, IL: Charles C Thomas; 1983.

2. Podgorsak EB. Radiation physics for medical physicists. 2nd ed. Heidelberg, Germany: Springer; 2010.

3. Nath R, Anderson LL, Luxton G, Weaver KA, Williamson JF, Meigooni AS. Report of AAPM Radiation Therapy Committee Task Group 43: Dosimetry of Interstitial Brachytherapy Sources [Electronic Version]. Med Phys. 1995;22(2):209–34.

4. Rivard MJ, Coursey BM, DeWerd LA, Hanson WF, Huq MS, Ibbott GS, et al. Update of AAPM Task Group No. 43 Report: A revised AAPM protocol for brachytherapy dose calculations [Electronic Version]. Med Phys. 2004;31(3):633–74.

5. Venselaar J, Meigooni AS, Baltas D, Hoskin P, editors. Comprehensive brachytherapy: physical and clinical aspects. Boca Raton, FL: CRC Press, Taylor and Francis Group.

6. Perez-Calatayud J, Ballester F, Das RK, DeWerd LA, Ibbott GS, Meigooni AS, et al. Dose calculation for photon-emitting brachytherapy sources with average energy higher than 50 keV: Report of the AAPM and ESTRO [Electronic Version]. Med Phys. 2012;39(5):2904-2929.

7. Williamson JF, Li Z. Monte Carlo aided dosimetry of the microselectron pulsed and high dose-rate 192Ir sources [Electronic Version]. Med Phys. 1995;22(6):809–19.

8. Daskalov GM, Loffler E, Williamson JF. Monte Carlo-aided dosimetry of a new high dose-rate brachytherapy source [Electronic Version]. Med Phys. 1998;25(11):2200–8.

9. Granero D, Vijande J, Ballester F, Rivard MJ. Dosimetry revisited for the HDR 192Ir brachytherapy source model mHDR-v2 [Electronic Version]. Med Phys. 2011;38(1):487–94.

10. van Veelen B, Ma Y, Beaulieu L. ACE: Advanced Collapsed cone Engine (White Paper). White Paper Elekta. 2014;1–16.

11. Carlsson AK, Ahnesjö A. The collapsed cone superposition algorithm applied to scatter dose calculations in brachytherapy [Electronic Version]. Med Phys. 2000;27(10):2320–32.

12. Carlsson Tedgren AK, Ahnesjö A. Accounting for high Z shields in brachytherapy using collapsed cone superposition for scatter dose calculation [Electronic Version]. Med Phys. 2003;30(8):2206–17.

13. DeWerd LA, Ibbott GS, Meigooni AS, Mitch MG, Rivard MJ, Stump KE, et al. A dosimetric uncertainty analysis for photon-emitting brachytherapy sources: report of AAPM Task Group No. 138 and GEC-ESTRO [Electronic Version]. Med Phys. 2011;38(2):782–801.

14. Zourari K, Pantelis E, Moutsatsos A, Sakelliou L, Georgiou E, Karaiskos P, et al. Dosimetric

accuracy of a deterministic radiation transport based 192Ir brachytherapy treatment planning system. Part III. Comparison to Monte Carlo simulation in voxelized anatomical computational models [Internet Version]. Med Phys. 2013;40(1):11712.

15. Ballester F, Carlsson Tedgren Å, Granero D, Haworth A, Mourtada F, Fonseca GP, et al. A generic high-dose rate 192Ir brachytherapy source for evaluation of model-based dose calculations beyond the TG-43 formalism [Internet Version]. Med Phys. 2015;42(6):3048–62.

16. Beaulieu L, Carlsson Tedgren A, Carrier J-F, Davis SD, Mourtada F, Rivard MJ, et al. Report of the Task Group 186 on model-based dose calculation methods in brachytherapy beyond the TG-43 formalism: Current status and recommendations for clinical implementation [Electronic Version]. Med Phys. 2012;39(10):6208.

17. Moura ES, Micka JA, Hammer CG, Culberson WS, DeWerd LA, Rostelato MECM, et al. Development of a phantom to validate high-dose-rate brachytherapy treatment planning systems with heterogeneous algorithms [Electronic Version]. Med Phys. 2015;42(4):1566–74.

18. Sharma R, Jursinic PA. In vivo measurements for high dose rate brachytherapy with optically stimulated luminescent dosimeters [Electronic Version]. Med Phys. 2013;40(7):71730.

19. Petrokokkinos L, Moutsatsos A, Karaiskos P, Kouridou V, Pantelis E, Papagiannis P, et al. On the use of VIP gel dosimetry in HDR brachytherapy [Electronic Version]. J Phys Conf Ser. 2009;164:12051.

20. Subhalaxmi M, Selvam TP. Monte Carlo-based investigation of absorbed-dose energy dependence of radiochromic films in high energy brachytherapy dosimetry [Electronic Version]. J Appl Clin Med Phys. 2014;15(1):4448.

21. Sutherland J. Monte Carlo calculated absorbed-dose energy dependence of EBT and EBT2 film [Electronic Version]. Med Phys. 2010;37(3):1110–6.

22. Massillon-JL G, Chiu-Tsao S-T, Domingo-Muñoz I, Chan MF. Energy Dependence of the New Gafchromic EBT3 Film: Dose Response Curves for 50 KV, 6 and 15 MV X-Ray Beams [Electronic Version]. Int J Med Physics,Clinical Eng Radiat Oncol. 2012;1(2):60–5.

23. Niroomand-Rad A, Blackwell CR, Coursey BM, Gall KP, Galvin JM, Mclaughlin WL, et al. Radiochromic film dosimetry: recommendations of AAPM radiation therapy committee task group no. 55 [Electronic Version]. Med Phys. 1998;25(11).

24. Rink A. Point-based ionizing radiation dosimetry using radiochromic materials and a fiberoptic readout system. Vol. 1, Ph.D Thesis. University of Toronto, Canada; 2008.

25. Lewis D, Micke A, Yu X, Chan MF. An efficient protocol for radiochromic film dosimetry combining calibration and measurement in a single scan [Electronic Version]. Med Phys. 2012;39(10):6339.

26. Ramos Garcia LI, Perez Azorin JF. Improving the calibration of radiochromic films by the use of uncertainties in optical density and dose [Electronic Version]. Med Phys. 2013;40(7).

27. Micke A, Lewis DF, Yu X. Multichannel film dosimetry with nonuniformity correction [Electronic Version]. Med Phys. 2011;38(5):2523–34.

28. Galantai A. The theory of Newton' s method [Electronic Version]. J Comput Appl Math. 2000;124:25–44.

29. Taylor BN, Kuyatt CE. NIST Technical Note 1297 1994 Edition, Guidelines for Evaluating and Expressing the Uncertainty of NIST Measurement Results. National Institute of Standards and Technology. 1994.

30. Morrison H, Menon G, Sloboda RS. Radiochromic film calibration for low-energy seed brachytherapy dose measurement [Electronic Version]. Med Phys. 2014;41(7):72101.

31. Chiu-Tsao S-T, Medich D, Munro J. The use of new GAFCHROMIC EBT film for 125I seed dosimetry in Solid Water phantom [Electronic Version]. Med Phys. 2008;35(8):3787–99.

Chapter 3 – Experimental Assessment of ACE for a Multi-channel Vaginal Cylinder Applicator

3.1 – Introduction

As stated previously, the use of MDBCAs with gynecological applicators has been investigated for some applicator models. However, the performance of MDBCAs has not yet been reported for a multi-channel vaginal cylinder (MCVC). Therefore, we present an experimental evaluation of OcB ACE v4.5 for a MCVC applicator using radiochromic film measurements. This evaluation focuses on ACE's ability to predict dose variations at the applicator surface caused by applicator-based heterogeneities. Differences between ACE calculated doses and the clinical standard TG-43 are used to evaluate the clinical implications of using ACE to predict heterogeneity-induced dose variations. A thorough and valid evaluation of ACE required supplementary work, including micro-CT imaging and MC simulations, to explain observed dose variations. The methods used for these investigations and the origins of dose variations are described.

3.2 – Materials and Methods

3.2.1 – Film, Applicators, and Oncentra® Brachy

All film measurements were performed using Gafchromic™ EBT3 film (Ashland Specialty Ingredients, Wayne, NJ, lot #03181303 and #04201501). Triple channel film dosimetry was performed (Section 2.2.2) with calibration curves determined separately for each film batch. Film measurements were made at the surface of a 35 mm diameter Vaginal CT/MR MCVC (Elekta, Stockholm, Sweden, part #110.761) with a vaginal tube (part #101.002), which is shown in Figure 3.1a and 3.1b. It has eight peripheral channels, and a vaginal tube may be inserted into the MCVC to provide a central channel. There are two 5 mm deep grooves on the outside of the applicator where a perineal bar can be attached to provide fixation (Figure 3.1b). The grooves begin 60 mm from the tip of the applicator. The majority of the applicator is composed of polyphenylsulfone (PPSU)

plastic, which has a mass density of 1.29 g/cc. For comparison, film measurements were also made on the surface of a 35 mm diameter single-channel vaginal cylinder (VC) applicator (Elekta, Stockholm, Sweden, part #084.350). The VC applicator consisted of five 2 cm long cylinder segments, in addition to a dome shaped end piece, arranged on a central stainless steel catheter (Figure 3.1c). OcB v4.5 (Elekta, Stockholm, Sweden) with the TG-43 formalism was used for planning the film irradiations, and dose was delivered using an HDR Ir-192 microSelectron® v3 afterloader (Elekta, Stockholm, Sweden).

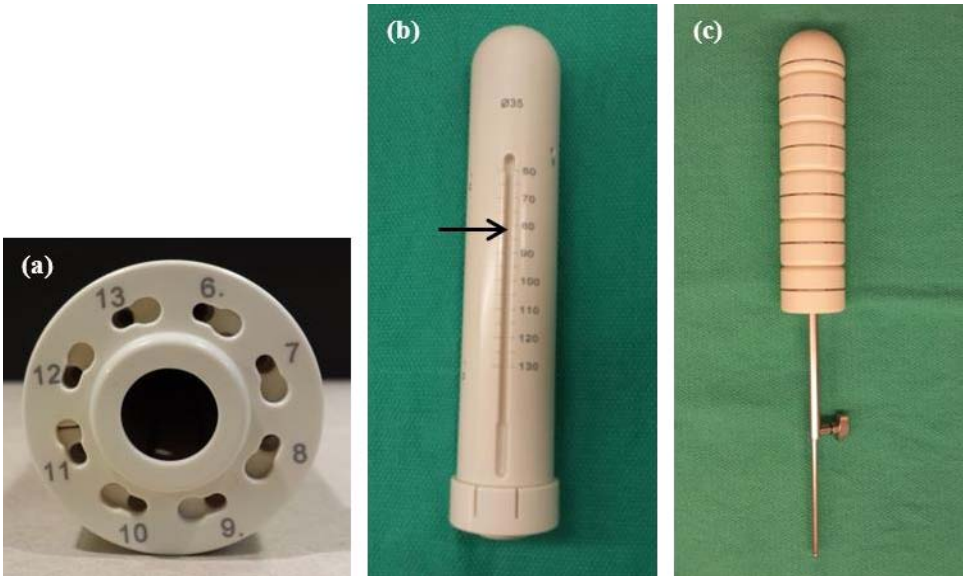

Figure 3.1 – An axial view of the multichannel vaginal cylinder (a), a full view of the MCVC with an outer groove visible (identified with an arrow) (b), and the single-channel vaginal cylinder applicator with five cylindrical segments (c).

3.2.2 – Radiochromic Film Measurements

Using the MCVC model available in the applicator library of the OcB software, a dose of 500 cGy was prescribed to a set of dose points on the surface of the applicator, over a 70 mm length. To isolate dosimetric effects caused by heterogeneities, it was desirable to prescribe as uniform a dose as possible to the surface of the applicator. Along the length of the applicator, prescription points were placed every 5 mm between 60 mm and 130 mm from the applicator tip, and at every 22.5

degrees around the circumference of the applicator, for a total of 240 points. Two different sets of dwell positions were used: positions activated only in the central channel, or only in the peripheral channels of the applicator. When the central channel was loaded, 20 dwell positions spaced 5 mm apart were activated, with the first dwell position 50 mm from the applicator tip. When the peripheral channels were loaded, 136 dwell positions (17 per channel) spaced 5 mm apart were activated, with the first dwell position 54 mm from the applicator tip. The dose was geometrically optimized on the surface of the applicator.

Film measurements were made at the surface of the MCVC applicator by wrapping a 20 cm long film piece around the outside of the applicator. The film was held in place with a 3 mm thick acrylic cylindrical sleeve whose inner radius was 0.5 mm larger than the applicator. Irradiations using the MCVC applicator were performed in a 30x30x30 cm^3 water tank with the applicator oriented vertically (Figure 3.2). The dose was delivered to the film under two conditions: the applicator was either placed in the water prior to being inserted into the sleeve and film to ensure the applicator grooves were filled with water, which will be referred to as the "water-in-grooves" set-up, or the film and sleeve were affixed to the applicator prior to insertion into the water and a tight waterproof latex sleeve was placed around the applicator to ensure water did not enter the grooves, which will be referred to as the "air-in-grooves" set-up.

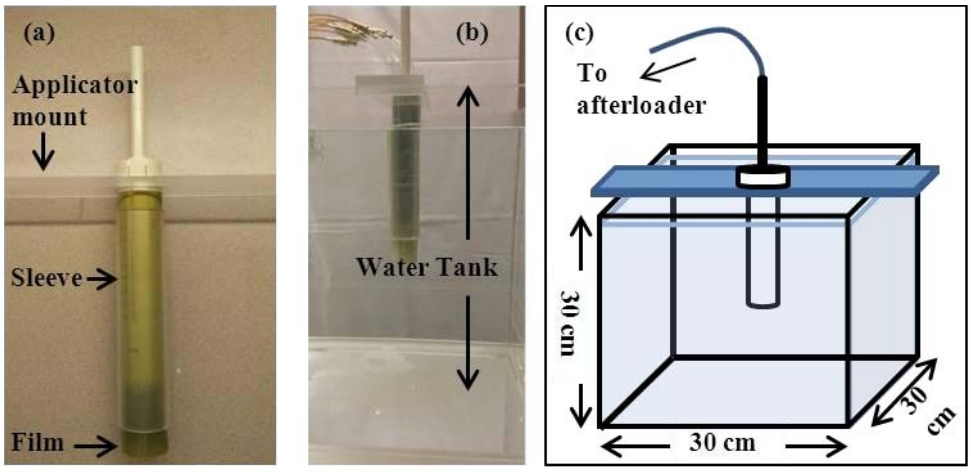

Figure 3.2 – The multichannel vaginal cylinder with Gafchromic™ film wrapped around the exterior and held in place by an acrylic sleeve (a). The applicator with film placed in the 30x30x30 cm^3 water tank (b). A schematic of the 30x30x30 cm^3 water tank (c).

For comparison purposes, this experimental methodology was repeated with the 35 mm diameter single-channel VC applicator. Treatment planning was performed on CT images of the VC applicator because an applicator model was not available in the OcB applicator modeling library. A uniform dose of 500 cGy was prescribed to the surface of the VC applicator using dose points placed along four opposing sides of the applicator.

For the doses obtained from film measurements, an IS correction was applied to the dose values to account for the thickness of the film, which relocates the measurements to the surface of the applicator. When the central channel was used, the IS correction equated to a multiplicative factor of $(17.635/17.5)^2$. When the peripheral channels were used, the IS correction for a point on the surface of the applicator was determined by a weighted average of the individual IS corrections from all dwell positions. IS corrections were calculated for 16 points at different azimuthal angles on the surface of the applicator. The average IS correction was 1.0087 ± 0.0006, which was applied to the peripheral channel film measurements. Dose profiles were then taken across the film to investigate the variation in dose around the surface of the applicator. The dose profiles were averaged over a length of 100 pixels (35.3 mm centered on the prescribed dose region) and

obtained using a moving average width of 5 pixels (1.8 mm) with respect to the dose maps. The horizontal moving average was performed to account for the film possibly being slightly tilted during irradiation or scanning. An average dose was calculated from the same area of the film used to obtain the averaged profiles. The averaged dose profiles were also used to obtain values for dose variations across the surface of the applicator: the maximum dose variation was calculated as the difference between the minimum and maximum doses; the size of the largest peak refers to the height of the dose difference observed at the locations of the two grooves in the applicator; and the baseline variation is the difference between the minimum and maximum doses at locations other than the peaks at the grooves or peripheral channels of the MCVC.

3.2.3 – Micro-CT Imaging

To adequately compare ACE to experimental film measurements, the MCVC applicator library model in OcB must be verified against the physical MCVC applicator. Additionally, initial film measurements revealed a non-uniform and slightly lower average dose at the applicator surface compared to TG-43. To further investigate the origin of the dose variations and verify the applicator model, micro-CT (μCT) images were obtained of the MCVC applicator, using a Siemens Inveon™ Hybrid Micro-PET/CT Scanner (Siemens, Knoxville, TN). The images were used to accurately measure the dimensions and geometry of the applicator, film, and sleeve, which could contribute to deviations in the measured dose from the prescribed dose. The images had isotropic voxels with a side length of 31μm. Image analysis was performed using ImageJ v1.49 (National Institutes of Health, USA).

3.2.4 – TG-43 and ACE Dose Calculations

The TG-43 and ACE dose calculations, computed in OcB v4.5, were compared for the 35 mm MCVC applicator library model. The applicator was placed in a 30x30x30 cm^3 virtual water box with a 34.8 mm diameter cylinder of air centered on the applicator to emulate the outer grooves filled

with air. The cylinder of air was not made to have a 35 mm diameter to ensure the prescription dose points lay within the water and not air. ACE calculations were also performed with the outer grooves filled with water. Following the same procedure as in the experimental measurements, TG-43 was used to prescribe a dose of 500 cGy to a set of dose points on the surface of the applicator, over a 70 mm length. Two different sets of dwell positions were used: dwell positions activated only in the central channel, or only in the peripheral channels of the applicator. The activated dwell positions were the same as in the experimental plan. The dose was geometrically optimized on the surface of the applicator. The relative weightings of the dwell times when the central channel was loaded were identical to those used in the plan for the film measurement. When the peripheral channels were used, the doses to the prescription points on the surface of the applicator differed by an average of 0.04% from the doses to the same prescription points in the experimental plan. The dose was then recalculated using the sACE and hACE algorithms for the same dwell times. Additionally, with assistance from the vendor we increased the innermost margin of the sACE calculation from 10 mm to 20 mm (see Table 2.1). The sACE calculation was repeated for the central channel with this increased margin, which will be referred to as the sACE-20mm calculation. To evaluate the clinical relevance of dose variations predicted by ACE, TG-43 and ACE dose calculations were compared using point dose percent differences (Equations 3.1 and 3.2). In Equations 3.1 and 3.2, $\Delta D_{sACE\text{-}TG43}$ is the percent difference between the sACE calculated dose (D_{sACE}) and the TG-43 calculated dose (D_{TG43}), and $\Delta D_{hACE\text{-}TG43}$ is the percent dose difference between the hACE calculated dose (D_{hACE}) and D_{TG43}.

$$\Delta D_{sACE-TG43}\,(\%) = 100 \times \frac{D_{sACE}-D_{TG43}}{D_{TG43}} \tag{3.1}$$

$$\Delta D_{hACE-TG43}(\%) = 100 \times \frac{D_{hACE}-D_{TG43}}{D_{TG43}} \tag{3.2}$$

To investigate the dose on the surface of the applicator, points were placed every 22.5 degrees around its circumference, with a spacing of 5 mm along its length. The surface dose was averaged at

nine locations along the length of the applicator for each angle, covering a span of 40 mm centered in the area that the dose was prescribed to. Uncertainties are calculated according to the method described in Section 2.1.4. The averaged dose profiles were also used to obtain values for dose variations across the surface of the applicator: the maximum dose variation was calculated as the difference between the minimum and maximum doses; peak dose increases were calculated by subtracting the average dose for dose points not at peaks from the dose at the peak.

3.2.5 – Monte Carlo Calculations

3.2.5.1 – Water Equivalence of PPSU Plastic

The lower average dose at the applicator surface was also investigated by verifying the water equivalence of PPSU plastic. A MC simulation was performed in MCNP6 (version 1.0) with a single Ir-192 source placed in the center of a PPSU cylinder (1). The Ir-192 source was a simplified version of the mHDR-v2r source (Nucletron B.V., Veenendaal, The Netherlands) described by Granero *et al*. (2), for which the beveled edges and source wire were not included. The MCVC applicator was modelled as a 35 mm diameter cylinder with a length of 170 mm. Along the axis of the cylinder, a 2.7 mm diameter cylinder of air was placed to model the central channel of the applicator. The applicator was placed in a 30 cm radius sphere of water. The kerma to a cylindrical shell, which was 0.1 mm thick and 0.1 mm wide, placed directly on the surface of the applicator, was calculated using 10^9 particle histories. In MCNP6, "tallying" refers to the process of scoring parameters of interest. The F6 tally was used to score/calculate kerma in terms of MeV/g. MCNP6 was run in Mode P (mode photon) with the MCNPLIB84 photon cross-section library. The kerma was equated to dose, and was also calculated with the applicator cylinder composed of water for comparison to the dose calculated with the applicator composed of PPSU plastic.

3.2.5.2 – Experimental Scatter Conditions

The length of the applicator surface to which dose was prescribed was completely submerged in water, as seen in Figure 3.2b. However, part of the applicator protrudes out of the water and full scatter conditions are not achieved. The effect of incomplete scatter conditions on the dose to the surface of the applicator was investigated with a MC simulation in MCNP6. The geometry in the MC simulation represented the experimental measurement set-up. The previously described model of the MCVC applicator (Section 3.2.4.1) was placed in a water box with dimensions 30x30x28 cm^3 (same size water column as in the experimental water tank, which was not filled to the top). Twenty simulations were performed with the Ir-192 source located in the twenty different dwell positions used for experimental measurements. The source positions extended from the top edge of the water box to 9.5 cm into the water box. A 40 cm radius sphere of air surrounded the water box and applicator. The dose to a 0.1 mm thick and 35 mm long cylindrical shell, placed directly on the surface of the applicator and centered longitudinally on the prescribed dose area used in the experiment, was determined using 10^9 particle histories for each source location. Each of the 20 doses was weighted according to the experimental dwell weights to determine a total weighted dose. The simulations were repeated with the sphere of air assigned as water for comparison purposes.

3.3 – Results

All uncertainties are stated with a coverage factor of 2 (k=2).

3.3.1 – Radiochromic Film Measurements

Table 3.1 summarizes dose variations observed around the circumference of the applicator, which were obtained from the longitudinally averaged dose profiles taken across the film. The dose maps obtained from the film measurements are given in Figure 3.3. The dose maps are oriented such that the base of the applicator (bottom of Figure 3.1b and 3.1c) is at the top of the page. Figures 3.3a and 3.3b show the measurements taken with the central channel of the MCVC applicator loaded. For the

measurement in Figure 3.3b, the outer grooves were filled with water, and no distinct dose increases are visible above the grooves. In contrast, Figure 3.3a shows the film measurements with air in the grooves, where an (11 ± 8)% increase in dose is seen just above the two grooves on the outside of the applicator. Figure 3.3c shows the film results for the irradiation performed using the peripheral channels of the MCVC, with air in the grooves. The maximum dose variation was 3% less than the variation produced when the central channel was loaded (Figure 3.3a). Additionally, the variation was more gradual. For the peripheral channel loading, the surface dose is very similar for the air-in-grooves and water-in-grooves setups.

All measurements with the MCVC having the central channel loaded showed baseline dose variations around the circumference of the applicator. This change in dose was on average (10 ± 4)% of the mean dose. The maximum dose variation around the circumference of the VC (Figure 3.3e) was (9 ± 4)% of the mean dose. In contrast, the measurements with the peripheral channels loaded did not show a similar baseline dose variation.

Table 3.1 – Dose variations around the circumference of MCVC and VC applicators as measured with Gafchromic EBT3 film. The values are calculated from the longitudinally-averaged dose profile data. Percentages are listed in parentheses below the absolute doses and are relative to the mean dose. Expanded uncertainties (k=2) are given.

Applicator	Channel(s)	Set-up type	Maximum dose variation [cGy] (%)	Size of largest peak [cGy] (%)	Baseline variation [cGy] (%)	Mean dose [cGy]
MCVC	Central	Water-in-grooves	49 ± 18 (11 ± 4)	N/A	49 ± 18 (11 ± 4)	464 ± 16
MCVC	Central	Air-in-grooves	77 ± 40 (16 ± 8)	54 ± 36 (11 ± 8)	37 ± 40 (8 ± 8)	477 ± 28
MCVC	Peripheral	Water-in-grooves	57 ± 26 (12 ± 6)	N/A	N/A	477 ± 14
MCVC	Peripheral	Air-in-grooves	61 ± 38 (13 ± 8)	N/A	N/A	476 ± 30
VC	Central	———	42 ± 20 (9 ± 4)	N/A	42 ± 20 (9 ± 4)	465 ± 14

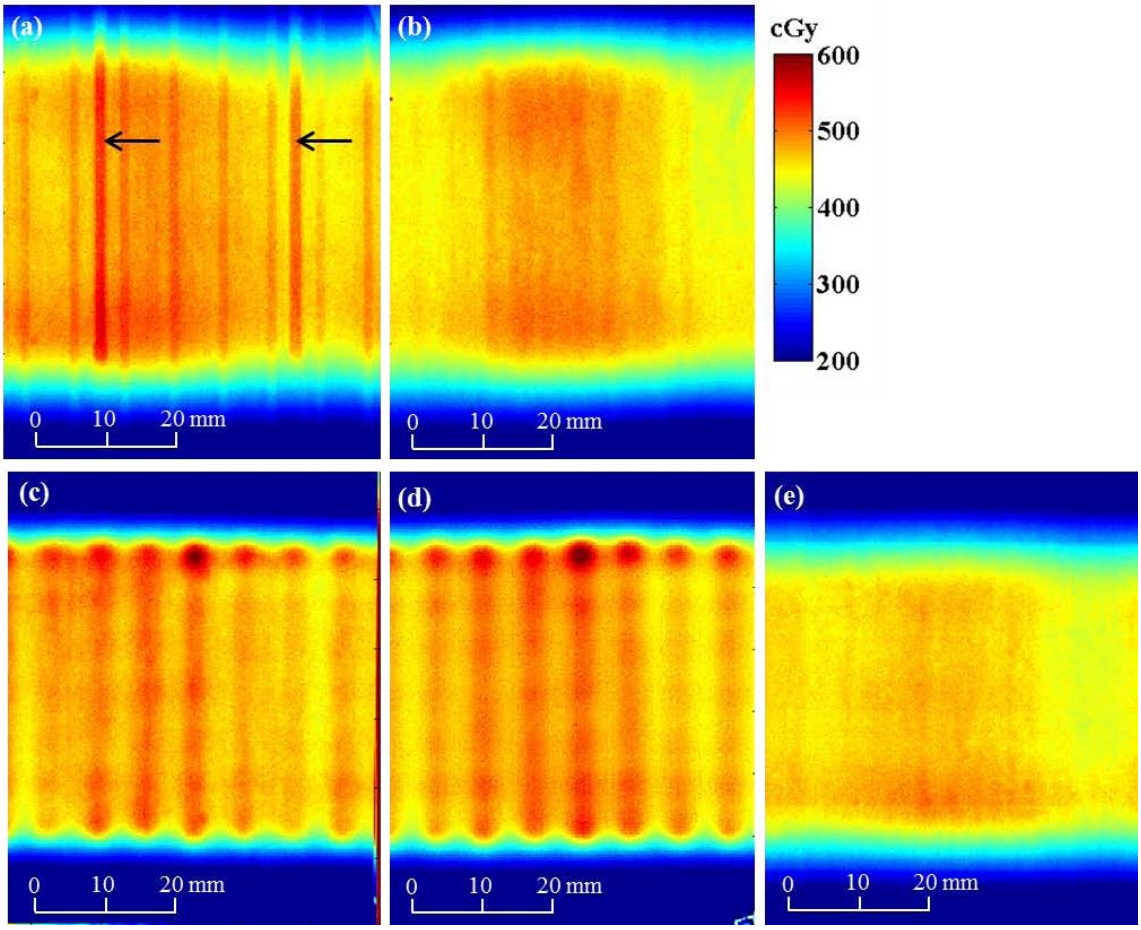

Figure 3.3 – Film measurements taken at the surface of: (a) the MCVC with the central channel loaded and air-in-grooves (identified with arrows); (b) the MCVC with the central channel loaded and water-in-grooves; (c) the MCVC with the peripheral channels loaded and air-in-grooves; (d) the MCVC with the peripheral channel loaded and water-in-grooves; (e) the VC.

3.3.4 – Micro-CT imaging

The μCT images of the MCVC applicator (Figure 3.4) revealed a central channel diameter of (2.69 ± 0.04) mm, which is greater than the expected 2.5 mm given in the OcB applicator library model. The outer diameter of the applicator was measured to be (35.07 ± 0.04) mm, which confirms the

diameter in the library model. Additionally, the distance between the applicator and the film varied slightly around the circumference of the applicator and was 0.2 mm at its maximum.

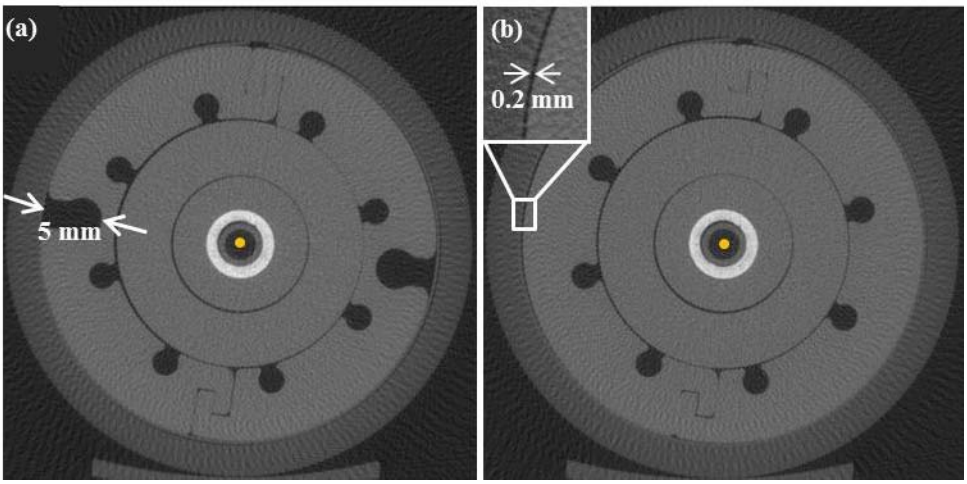

Figure 3.4 – μCT cross-sectional slices of the MCVC applicator with the vaginal tube, and film wrapped around the applicator and held in place with the acrylic sleeve. The central yellow dot is scaled to represent the microSelectron-HDR® Ir-192 v2 source with a 0.9 mm diameter. The images reveal a groove depth of 5 mm (a), and a maximum air gap between the applicator and the film of 0.2 mm (inset b).

3.3.3 – Water equivalence of PPSU plastic

The MC simulations found the average dose at the applicator surface for the PPSU applicator to be (0.8 ± 0.2)% lower than that for the water applicator.

3.3.4 – Experimental scatter conditions

The MC simulations found the average dose at the applicator surface for the experimental scatter conditions to be (1.015 ± 0.004)% lower than that for the full scatter conditions.

3.3.5 – TG-43 and ACE Dose Calculations

Percent dose differences between TG-43, sACE, sACE-20mm, and hACE calculations are given in Figure 3.5 for the library model of the MCVC applicator having air in the surface grooves. The

percent dose difference maps in Figure 3.5 are for an axial slice through the applicator, located in the middle of the length where the dose was prescribed on the applicator surface. In Figure 3.5a and 3.5b, a negative dose difference indicates that sACE predicts a lower dose than TG-43. The mean dose difference at the surface of the applicator between TG-43 and sACE or hACE, when the peripheral channels of the MCVC are loaded, is less than 4 %. This is also observed in Figures 3.6a and 3.6b, which plot the average dose to points on the surface of the applicator vs. azimuthal angle when the peripheral channels are loaded. sACE and hACE predict doses within 1% of each other to the surface of the applicator, which are on average (3 ± 8)% less than the doses predicted by TG-43. The ACE calculation margins are clearly visible in Figures 3.5a to 3.5e. In Figure 3.5a, the grid size transition from 1 mm to 2 mm is seen as the smaller square surrounding the applicator. The transition to 2 mm and 5 mm grid sizes, for hACE and sACE respectively, is seen as the larger square in all panels of Figure 3.5.

When the central channel is loaded (Figure 3.5b and 3.5c), sACE predicts an increase in dose above the two outer grooves on the surface of the applicator. However, sACE predicts this dose increase to points that are at least 1 mm off the surface of the applicator, not directly on the surface of the applicator. hACE (Figure 3.5e) does predict this dose increase to points directly on the surface of the applicator, as shown in Figure 3.6c, where a (6 ± 8)% increase in dose is seen above the two outer grooves compared to points not above the grooves. The sACE-20mm calculation (Figure 3.5c) also predicts a (6 ± 8)% increase in dose directly above the two outer grooves. TG-43 cannot predict this dose increase. Dose variations and mean doses to points on the surface of the applicator, as calculated by TG-43, sACE, sACE-20mm, and hACE, and measured by film, are summarized in Table 3.2.

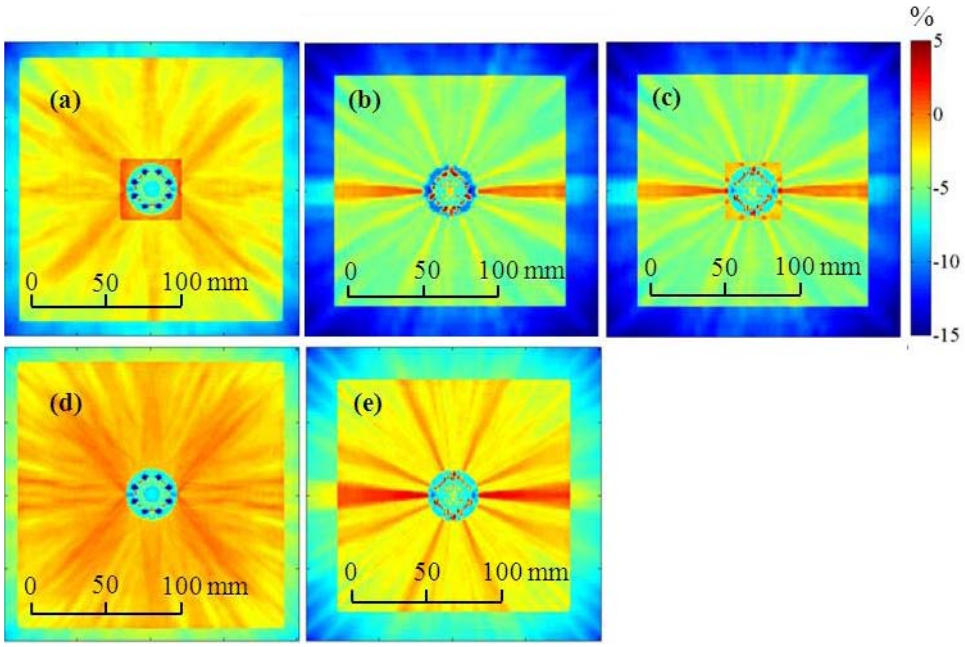

Figure 3.5 – Percent dose differences between the sACE and TG-43 dose calculations for a MCVC applicator having air in the surface grooves with the peripheral channels loaded (a), with the central channel loaded (b), and with the central channel loaded and the innermost margin increased from 10 mm to 20 mm (c). Percent dose differences between the hACE and TG-43 dose calculations for the MCVC with the peripheral channels loaded (d) and with the central channel loaded (e). The surface grooves lie in the horizontal plane bisecting the applicator. Positive percent differences indicate that ACE is calculating a higher dose than TG-43.

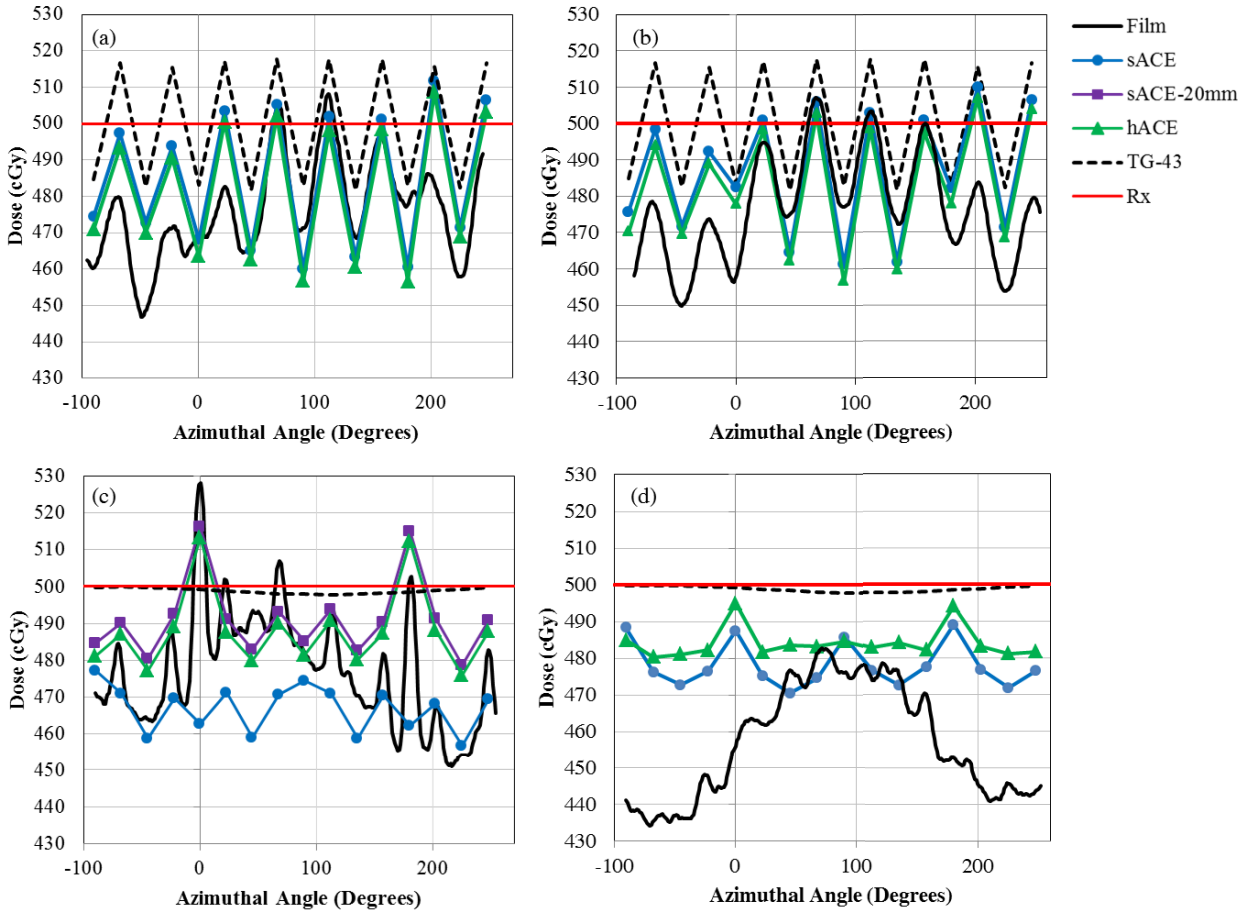

Figure 3.6 – The average dose to points on the surface of the MCVC applicator for the air-in-grooves set-up with the peripheral channels loaded (a), the water-in-grooves set-up with the peripheral channels loaded (b), the air-in-grooves set-up with the central channel loaded (c), and the water-in-grooves set-up with the central channel loaded (d). The dose is calculated using TG-43, sACE, sACE-20mm, and hACE using the same dwell times corresponding to a prescription dose of 500 cGy (TG-43) to the surface of the applicator. Data points at 0° and 180° are above the two outer grooves on the surface of the applicator. The red line indicates the prescribed dose of 500 cGy. The average dose measured by radiochromic film on the surface of the MCVC applicator is also given.

Table 3.2 – Dose variations around the circumference of the MCVC applicator calculated using TG-43, sACE, sACE-20mm, hACE, and measured using film. Percentages are relative to the mean dose and are given in parentheses. Expanded (k=2) uncertainties are given.

Channel/s	Material in grooves	Calculation/ measurement method	Maximum Dose variation [cGy] (%)	Mean Dose (cGy)	Dose calc. time (min)	# of transport directions (Primary/ residual)
Central	Air	sACE	20 ± 66 (4 ± 14)	467 ± 46	3	320/180
Central	Air	sACE-20mm	38 ± 68 (8 ± 14)	491 ± 50	4	320/180
Central	Air	hACE	37 ± 70 (8 ± 14)	488 ± 48	35	720/240
Central	N/A	TG-43	2 ± 48 (0 ± 10)	499 ± 35	N/A	N/A
Central	Air	Film	77 ± 40 (16 ± 8)	477 ± 28	N/A	N/A
Central	Water	sACE	18 ± 68 (4 ± 14)	478 ± 48	3	320/180
Central	Water	hACE	15 ± 70 (3 ± 14)	484 ± 48	35	720/240
Central	Water	Film	49 ± 18 (11 ± 4)	464 ± 16	N/A	N/A
Peripheral	Air	sACE	52 ± 68 (11 ± 14)	485 ± 48	28	240/128
Peripheral	Air	hACE	52 ± 68 (11 ± 14)	482 ± 48	286	500/200
Peripheral	Air	TG-43	36 ± 48 (7 ± 10)	500 ± 35	N/A	N/A
Peripheral	Air	Film	61 ± 38 (13 ± 8)	476 ± 30	N/A	N/A
Peripheral	Water	sACE	49 ± 68 (10 ± 14)	487 ± 48	28	240/128
Peripheral	Water	hACE	50 ± 68 (10 ± 14)	483 ± 48	286	500/200
Peripheral	Water	Film	57 ± 26 (12 ± 6)	477 ± 14	N/A	N/A

3.4 – Discussion

This section will discuss and explain dosimetric phenomena observed with the MCVC applicator film measurements, and evaluate the ability of ACE to predict these phenomena. When the peripheral channels of the MCVC were loaded, a uniform oscillation in dose was measured at the surface of the applicator (Figures 3.6a and 3.6b). This dose variation is not associated with a heterogeneity; it is an expected variation due to the proximity of the peripheral channels to the surface of the applicator not being able to create a perfectly uniform dose distribution, and is therefore predicted by TG-43 calculations. With the peripheral channels loaded, the maximum dose variation as determined by sACE and hACE was (11 ± 14)% of the mean dose, and is within the uncertainty of the measured dose variation of (13 ± 8)% of the mean dose. TG-43 calculations yielded a maximum dose variation of (7 ± 10)% of the mean dose.

There was a measured increase of (11 ± 8)% in the mean dose at the surface of the applicator above the two outer grooves when they are filled with air. This dose increase was also observed with hACE calculations and was (6 ± 8)% of the mean dose (Figure 3.6c). sACE did not predict a dose increase above the two outer grooves to points that are on the surface of the applicator, but did predict a dose increase of 6% at a distance of at least 1 mm off the surface of the applicator, as seen in Figure 3.5b. When the calculation was performed using sACE-20mm, such that the grid size at the surface of the applicator is 1 mm, the (6 ± 8)% increase in dose was seen at the surface of the applicator (Figure 3.6c). The 2 mm grid size of sACE will average the attenuation coefficients between the air and water, reducing the increase in dose at grid points right at the surface of the applicator. Additionally, dose points at a location not on the calculation grid are determined by trilinear interpolation between neighboring grid points. Therefore, depending on the alignment of the grid, the doses at the applicator surface could be averaged between doses in air and water. For vaginal vault HDR brachytherapy treatments at our center, a condom is usually placed around the applicator prior to insertion into the patient. Therefore, the applicator grooves

are not filled with fluids from the patient, which would likely result in peak dose variations similar to those observed in the film measurements. In pulsed dose rate (PDR) gynecological brachytherapy treatments, the longer treatment times require use of the perineal bars that slide about 2 cm into the grooves for immobilization of the applicator, and a condom is not placed around the applicator. In this case, the grooves may fill with bodily fluids from the patient causing a reduction or elimination of the peak dose variations.

In addition to the increased dose at the grooves, a baseline dose variation was measured around the surface of the MCVC applicator, which was also observed with the VC applicator. The average baseline dose variation for either water or air in the grooves of the MCVC applicator was (10 ± 4)% of the mean dose. This dose variation around the circumference of applicators is likely due to offset positioning of the source within the central channel. The MCVC applicator central channel has a diameter of 2.7 mm as measured from the μCT images, while the Ir-192 HDR v2 source has a diameter of 0.9 mm. When all dwell positions are in contact with the channel wall and the film is 0.2 mm off the surface of the applicator on the opposite side, the dose to the active layer of the film farthest from the dwell positions will be approximately 91% of the dose to the film closest to the dwell positions (largest possible offset), which corresponds to a difference of about 9% of the mean dose. This dose difference is computed using the average IS correction, weighted with respect to the dwell times for each dwell position, to a location midway down the irradiated portion of the applicator. Figure 3.7 illustrates the dimensions of the source and MCVC central channel.

Lastly, all of the film measurements yielded average doses 3% - 7% less than the prescribed dose calculated using TG-43. However, no measurements were found to yield statistically significant differences from TG-43. The water-in-grooves central channel film measurements yielded a dose that was (7 ± 8)% less than that for the TG-43 calculations. For the same condition, sACE and hACE calculations predicted doses (4 ± 12)% and (3 ± 12)% lower than TG-43 calculated

doses, respectively. When the central channel of the MCVC applicator was used and air was in the grooves, the average dose measured by the film was (4 ± 8)% lower than the TG-43 calculated dose of 500 cGy. When the peripheral channels of the MCVC were used, the film measured an average dose that was (5 ± 10)% lower than the TG-43 calculated dose; sACE and hACE predicted doses (3 ± 12)% and (4 ± 12)% lower. As shown by the MC simulations, the applicator material is expected to alter the dose distribution at the applicator surface, compared to water, by less than 1%. Additionally, the MC simulations showed that the experimental scatter conditions decrease the average surface dose by 1%. Therefore, the applicator material and scatter conditions may contribute to the average film dose being lower than the average TG-43 dose, but the lack of statistical significance doesn't allow for this to be confirmed. Overall, these modest average dose decreases can be attributed to measurement and calculation uncertainties and are not of clinical concern, in contrast to the dose increase observed above the MCVC grooves when they are filled with air.

The radiation oncologists at our clinic advise that a localized increase in dose of 11%, as observed above the two outer grooves when filled with air, would not constitute a significant clinical concern on its own. However, if the dose variation was to rise to above 20%, which is possible when combining the peak dose increase and baseline dose variation, it may necessitate adjustment of the plan. Another consideration that may contribute to a larger dose variation is the presence of air pockets surrounding the applicator, as studied by others (3–5). When considering TG-43 calculations alone, it was found that 11 out of 174 (6.3%) of patients were underdosed by an average of 6.1% of the prescribed dose due to displacement of the vaginal mucosa by air gaps (3). A phantom study by Maxwell *et al* (6) found that TG-43 slightly underestimates the dose due to the inhomogeneity caused by the presence of air – the dominant effect is a decreased dose to tissue due to increased distance from the source.

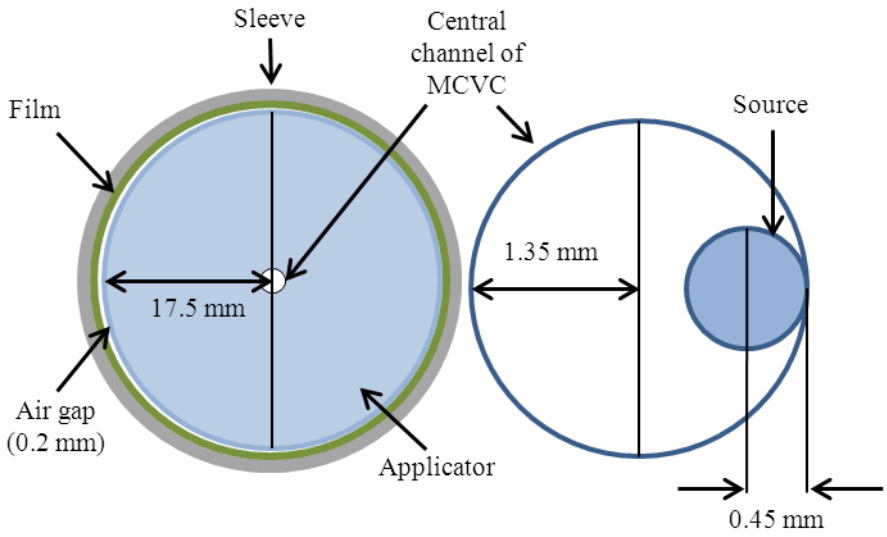

Figure 3.7 – Illustration of the worst case geometry for the Ir-192 source in the central channel of the MCVC for our film measurements. The combination of the source being at the edge of the central channel, and the 0.2 mm air gap between the applicator and film, causes a difference in dose at opposite sides of the applicator surface.

3.5 – Conclusion

Triple channel radiochromic film dosimetry was performed to verify Oncentra® Brachy ACE v4.5 calculations for a MCVC applicator, and comparisons between TG-43 and ACE dose calculations were used to evaluate the clinical significance of applicator-heterogeneity-induced dose variations. The hACE dose calculations were found to agree with the film measurements when just the central channel of the applicator was loaded and when just the peripheral channels of the applicator were loaded. The sACE calculations did not predict an increase in dose to the applicator surface above two outer applicator grooves when they were filled with air, and TG-43 calculations cannot predict this increase. When the peripheral channels are used, the agreement between sACE and hACE calculations at the surface of the applicator suggests that sACE is sufficient when dwell positions are located close to prescription points. The film measurements also revealed a baseline azimuthal dose variation on the applicator surface, likely due to non-axial positioning of the Ir-192 source in

the central channel, which could not be predicted by the ACE calculations. Clinical use of the MCVC applicator and ACE algorithm should take the dosimetric effects reported here into consideration within the context of a particular treatment being planned.

3.6 – References

1. Goorley T, James M, Booth T, Brown F, Bull J, Cox LJ. Initial MCNP6 Release Overview. Nucl Technol. 2012;180:298–315.

2. Granero D, Vijande J, Ballester F, Rivard MJ. Dosimetry revisited for the HDR 192Ir brachytherapy source model mHDR-v2 [Electronic Version]. Med Phys. 2011;38(1):487–94.

3. Onal C, Guler O, Dolek Y. The impact of air pockets around the vaginal cylinder on vaginal vault brachytherapy [Electronic Version]. Br J Radiol. 2015;88(1047):20140694.

4. Hassauna A, Abdulaziz Bahadur Y, Constantinescu C. Assessment of air pockets in high-dose-rate vaginal cuff brachytherapy using cylindrical applicators [Electronic Version]. J Contemp Brachytherapy. 2014;6(3):271–5.

5. Richardson S, Palaniswaamy G, Grigsby P. Dosimetric effects of air pockets around high-dose rate brachytherapy vaginal cylinders [Electronic Version]. Int J Radiat Oncol Biol Phys. 2010;78(1):276–9.

6. Maxwell A, Thiruthaneeswaran N, Lowe G, Wills R, Sripali S, Hoskin PJ. The Dosimetric Impact of Air in Vaginal Vault Brachytherapy [Electronic Version]. Brachytherapy. Elsevier Inc; 2016;15(2016):S104.

Chapter 4 – Experimental Assessment of ACE for Scalp Brachytherapy Treatments

4.1 – Introduction

The treatment of NMSC of the scalp using BT involves variably-sized tissue heterogeneities such as the presence of air gaps between the surface mold and skin, skin thickness, and skull thickness. The objective of the work reported here was to evaluate the ability of ACE to calculate dose for a range of heterogeneity sizes corresponding to clinically relevant situations. To accomplish this, we performed an experimental assessment of ACE for a variably configured, multi-layered slab phantom using radiochromic film measurements.

4.2 – Materials and Methods

4.2.1 – Film, Scalp Phantom, and Oncentra® Brachy

As described in Section 1.2.2, scalp BT treatments at our clinic are performed using a custom head mold to which the BT catheters are adhered. An experimental slab phantom was designed to model the components of the head (skin, skull, and brain) and mold using tissue-equivalent and water-equivalent plastic (Figure 4.1). The thicknesses of the layers were determined by examining the CT data sets of three different scalp patients for skin thickness, skull thickness, air gap size between the mold and head, and mold thickness (Table 4.1). Permission to use these retrospective images was obtained from the Health Research Ethics Board of Alberta Cancer Committee (Study ID: HREBA.CC-16-0657). Three variable parameters were selected for study: air gap between the mold and head, skin thickness, and skull thickness. These parameters were varied from a standard phantom configuration (phantom A), which was designed to resemble the most commonly observed parameters. Table 4.2 summarizes six variations of the slab phantom with varying thicknesses of the layers. The thicknesses of the layers were constrained by the thicknesses of the tissue-equivalent and water-equivalent plastic slabs available in our center. Measurements were

also performed in a phantom composed entirely of solid water (phantom W). Phantom W had the same layer thicknesses as phantom A, but with solid water replacing the skull- and brain-equivalent layers.

The tissue-equivalent and water-equivalent materials used in the phantoms are described in Table 4.3. The slabs were obtained from Gammex® (Sun Nuclear Corporation, Middleton, WI) and Scanplas Inc. (Orpington, Kent, UK). The composition of the brain material was not available, therefore it was approximated by results presented by the author who developed the Scanplas Inc. materials (1,2).

TG-43 and ACE calculations were performed in OcB v4.5. Material composition can be assigned to a region of interest by first contouring the region, then selecting a material from a library in OcB. ACE has two options for assigning mass densities to materials: either (i) using the Hounsfield Units (HU) from the CT images, or (ii) using OcB's pre-defined density for that material (uniform density assignment). ACE calculations that use HU, and ACE calculations that use uniform density assignment, will be referred to as ACE-HU and ACE-UNI, respectively. The dose was delivered using a HDR Ir-192 microSelectron® v3 afterloader (Elekta, Stockholm, Sweden).

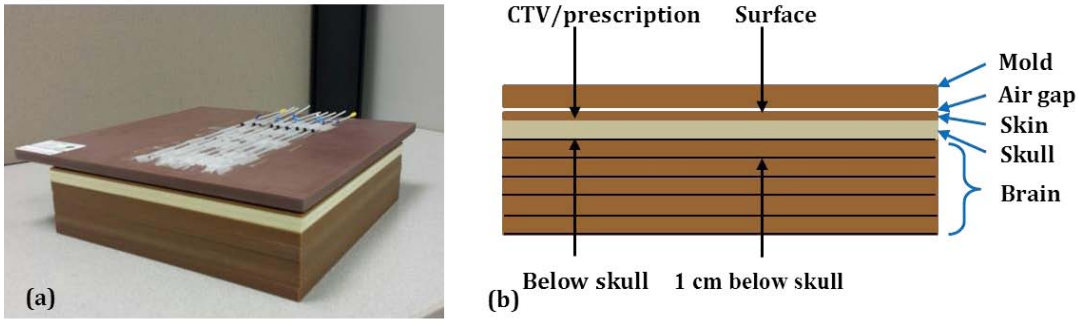

Figure 4.1 – Picture of slab phantom variation B (a), and interpretive schematic (b). The black arrows identify the locations of film placement, and the blue arrows identify the layers of the phantom.

Table 4.1 – Average patient anatomy and treatment parameters obtained from three clinical CT data sets.

Patient	Skull thickness[1] (mm)	Mold thickness[2] (mm)	Air gap[2] (mm)	Skin thickness[2] (mm)	CTV location on skull
A	10 ± 0	6 ± 1	5 ± 1	2 ± 0	Superior
B	7 ± 1	5 ± 1	5 ± 0	7 ± 1	Anterior
C	9 ± 0	9 ± 0	6 ± 1	5 ± 0	Posterior

[1]Below CTV.
[2]Along shortest path between catheters and CTV.

Table 4.2 – Thicknesses of the layers for the six different phantom variations A-F. The underlined numbers identify the parameter that is different from phantom A. The mold thickness was 10 mm and the brain thickness was 5 cm for all phantom variations.

Phantom	t_{air} (mm)	t_{skin} (mm)	t_{skull} (mm)
A	0	3	10
B	**3**	3	10
C	**5**	3	10
D	0	3	**5**
E	0	**1**	10
F	0	**5**	10

Table 4.3 – Elemental composition and mass densities of physical phantom materials and the materials used in OcB ACE calculations. The mass densities for OcB materials are only used by OcB-UNI calculations.

Material Name	Material Source	Phantom Layer	H (%)	C (%)	N (%)	O (%)	Z>8 (%)	Mass Density (g/cc)	CT Number in OcB* (HU)
Cortical Bone	OcB	Skull	3.4	15.5	4.2	43.5	Na(0.1), Mg(0.2), S(0.2), Cl(0.3), Ca(22.5)	1.92	1827
Hard Bone (SB5)	Scanplas	Skull	2.6	30.58	0.98	38.93	Cl(0.06), Ca(26.85)	1.87	910 ± 20
Solid Water	OcB	Mold and Skin	8.1	67.2	2.4	19.9	Cl(0.1), Ca(2.3)	1.04	30
Solid Water	Gammex	Mold	8.1	67.2	2.4	19.9	Cl(0.1), Ca(2.3)	1.04	61 ± 4
Solid Water	Scanplas	Skin	8.41	67.97	2.27	18.87	Cl(0.13), Ca(2.35)	1.00	61 ± 4
Heart	OcB	Brain	10.4	13.9	2.9	71.8	Na(0.1), P(0.2), S(0.2), Cl(0.2), K(0.3)	1.05	40
Brain	Woodard (1,2)	Brain	10.7	14.5	2.2	71.2	Na(0.2), P(0.4), S(0.2), Cl(0.3), K(0.3)	1.04	52 ± 4
Air	OcB	Air	—	—	75.5	23.2	Ar(1.3)	0.00121	-1000
Air	Physical	Air	—	—	—	—	—	—	-850 ± 20

*As specified in the OcB software, or from averaging HU data points in OcB. Uncertainties are stated with a coverage factor of 2 (k=2).

4.2.2 – Radiochromic Film Measurements

Planning was performed in a clinical version of OcB v4.5 using CT images obtained for each phantom variation using a Brilliance Big Bore CT Simulator (Philips N.V., Amsterdam, Netherlands). The scan parameters were the same as those used for clinical NMSC treatments: 2 mm slice thickness, 400 mAs, and 120 kVp. In OcB, 81 prescription points were placed in concentric circles at the skull-skin interface, covering a 5 cm diameter circular area – a typical size of the clinical target volume (CTV) in scalp BT treatments. A dose of 400 cGy was prescribed to these points using TG-43, and the dose was geometrically optimized. A typical treatment at our clinic includes 10 fractions

of 400 cGy to the CTV. The prescription area defined by the points will henceforth be referred to as the CTV.

For each phantom variation, radiochromic films were irradiated at four depths within the phantom: above the skin layer (surface), above the skull layer (CTV location), just below the skull layer, and 1 cm below the skull layer. For phantoms E and F, an additional film measurement was performed at the center of the skull layer to investigate the bone dose. Phantoms E and F were chosen because it was expected that they would result in different skull doses without introducing the additional variable of an air gap. Each film measurement was performed with a separate irradiation. Triple channel film dosimetry was performed as previously described in Section 2.2.2. All results from film measurements are stated as dose to water in medium ($D_{W,M}$).

To account for film thickness, an IS correction was applied to each film irradiation, which relocates the measurements to their respective locations specified in the previous section (Figure 4.1). An IS correction to a point in the phantom was determined by a weighted average of the individual IS corrections from all dwell positions, where weights for each IS equaled the individual dwell time divided by sum of all dwell times. IS corrections were determined for 17 points within a 2 cm diameter circular area, perpendicular to the central axis, at all four film irradiation levels. The average of these IS corrections, for a given film level, was applied to the film. As an example, the IS correction for phantom A, at the CTV location, was 1.005.

For a given film depth, percent dose differences between the film measurements and TG-43 calculations were determined from the average film and TG-43 doses within a 2 cm diameter circular area perpendicular to the CAX (Equation 4.1). $\overline{\Delta D}_{film(above\ skull)-TG43}$ is an average over the two film locations above the skull, and $\overline{\Delta D}_{film(below\ skull)-TG43}$ is an average over the two film locations below the skull.

$$\Delta D_{film-TG43} = 100 \cdot \frac{D_{film} - D_{TG43}}{D_{TG43}} \tag{4.1}$$

4.2.3 – TG-43 and ACE Dose Calculations

In a research version of OcB v4.5, 400 cGy was prescribed to the same prescription points, using the same dwell positions, as in the experimental plans. The TG-43 calculated doses to the prescription points were less than 0.1% different from the corresponding TG-43 calculated doses in the experimental plans, on average.

To confirm the accuracy of the film measurements, ACE and TG-43 calculations were performed in phantom W by assigning a uniform density to the phantom CT data set. For phantoms A-F, ACE-HU calculations were performed with the skin, air, skull, and brain layers contoured, and assigned to use the material compositions of solid water, air, cortical bone, and heart tissue, respectively (Table 4.3). Both sACE and hACE calculations were performed using the same dwell times as used for the TG-43 calculations.

Initial results revealed inconsistencies between the ACE calculations and the measured doses. To investigate these discrepancies, ACE-UNI calculations for phantoms A and B were performed with the skin, air, skull, and brain layers contoured, and assigned to use the mass density and material compositions of solid water, air, cortical bone, and heart tissue, respectively (Table 4.3). Cortical bone is the only type of bone available in the OcB material library. It has a mass density of 1.92 g/cc, which corresponds to a CT number of 1827 HU. In contrast, the average CT number of the Scanplas hard bone equivalent plastic is 910 HU.

Dose profiles through the central axis (CAX) of the phantoms (defined with respect to the CTV) were obtained from exported DICOM radiation therapy (RT) dose files by calculating the average dose within a 2 cm diameter circular area perpendicular to the CAX. Percent dose differences between TG-43 and ACE calculated doses were determined according to Equations 3.1 and 3.2. As well, a volume-averaged percent dose difference was determined for a 2 cm diameter cylinder centered on the phantom CAX and extending from the surface to 1 cm below the skull

($\overline{\Delta D}_{sACE-TG43}$ and $\overline{\Delta D}_{hACE-TG43}$). Uncertainties are propagated according to the method described in Section 2.1.4.

4.2.4 – Comparisons of Skull Dose

For the film measurements performed at the middle of the skull layer, the percent dose difference between the average hACE calculated dose (dose to medium in medium, $D_{M,M}$) and the average film measured dose ($D_{W,M}$), for a 2 cm diameter circular area, was determined according to Equation 4.2. The percent dose difference between the TG-43 calculated dose at the middle of the skull layer (dose to water in water, $D_{W,W}$) and film measured skull dose ($D_{W,M}$) were determined by Equation 4.3.

$$\Delta D_{film-hACE}(\%) = 100 \cdot \frac{D_{film}-D_{hACE}}{D_{hACE}} \tag{4.2}$$

$$\Delta D_{film(skull)-TG43}(\%) = 100 \cdot \frac{D_{film}-D_{TG43}}{D_{TG43}} \tag{4.3}$$

4.3 – Results

All uncertainties are stated with a coverage factor of k=2 or 95% confidence.

4.3.1 – Calculations and Film Measurements for Slab Phantom

Table 4.4 summarizes the average percent dose differences between TG-43 calculated doses and film measurements or ACE calculated doses. All results are stated with a coverage factor of k=2, or 95% confidence. The film measurements for phantom W were (3 ± 4)% lower than the TG-43 calculated doses, on average (Figure 4.2). The sACE-UNI and hACE-UNI doses were both (3 ± 12)% lower than the TG-43 calculated doses. The larger uncertainties for these percent differences are due to the propagated 3.4% and 5% uncertainties associated with the TG-43 and ACE calculated doses, respectively. For all the phantoms, the average film measured dose above the skull layer was not significantly different from the TG-43 or ACE calculated doses at 95% confidence. When only the film measurements below the skull layer were considered, the average film measured dose was

different from the TG-43 and ACE calculated doses at 95% confidence, for all phantoms. On average, sACE-HU and hACE-HU calculated doses were not significantly different from the TG-43 calculated doses for all phantoms. Figure 4.3 plots the CAX dose profiles for all phantom variations. The profiles show that the film measurements mostly agree with the TG-43 and ACE-HU calculations above the skull layer, but not below the skull layer.

The ACE-UNI calculations predicted lower average doses than TG-43. The CAX dose profiles in Figure 4.4 show that sACE-UNI and hACE-UNI predict a greater dose reduction below the skull compared to the ACE-HU calculations.

Table 4.4 – Average percent dose differences between TG-43 calculated doses and film measurements (excluding the bone dose, Equation 4.1), or TG-43 calculated doses and ACE calculated doses (Equations 3.1 and 3.2). Uncertainties are stated with a coverage factor of 2 (k=2).

Phantom	Set-up difference from phantom A	$\overline{\Delta D}_{film(above\ skull-TG43)}$ (%)	$\overline{\Delta D}_{film(below\ skull)-TG43}$ (%)	$\overline{\Delta D}_{sACE-HU-TG43}$ (%)	$\overline{\Delta D}_{hACE-HU-TG43}$ (%)	$\overline{\Delta D}_{sACE-UNI-TG43}$ (%)	$\overline{\Delta D}_{hACE-UNI-TG43}$ (%)
W	All solid water	-2 ± 5	-3 ± 6	———	———	-3 ± 12	-3 ± 12
A	No air gap, 3mm skin, 10 mm skull	2 ± 6	-8 ± 6	0 ± 12	1 ± 12	-3 ± 12	-2 ± 12
B	+ 3 mm air gap	2 ± 6	-7 ± 6	3 ± 12	3 ± 12	-1 ± 12	-1 ± 12
C	+ 5 mm air gap	-2 ± 6	-10 ± 6	0 ± 12	1 ± 12	———	———
D	- 5 mm skull	-3 ± 6	-8 ± 6	-1 ± 12	0 ± 12	———	———
E	- 2 mm skin	-1 ± 6	-8 ± 6	0 ± 12	0 ± 12	———	———
F	+ 2 mm skin	-1 ± 6	-9 ± 6	0 ± 12	1 ± 12	———	———

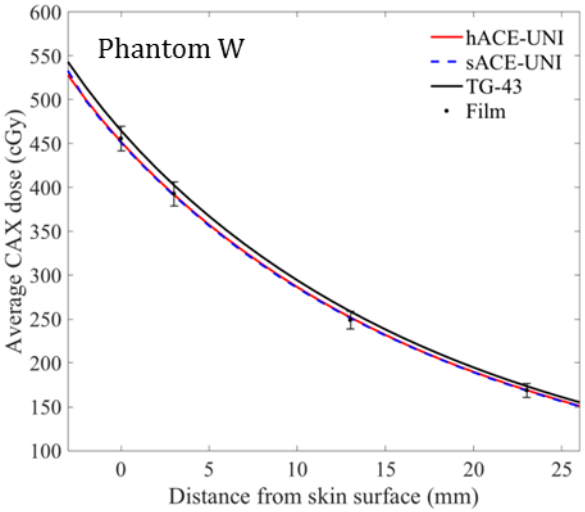

Figure 4.2 – Average CAX dose for phantom W as calculated by sACE-UNI, hACE-UNI, and TG-43, and measured by film.

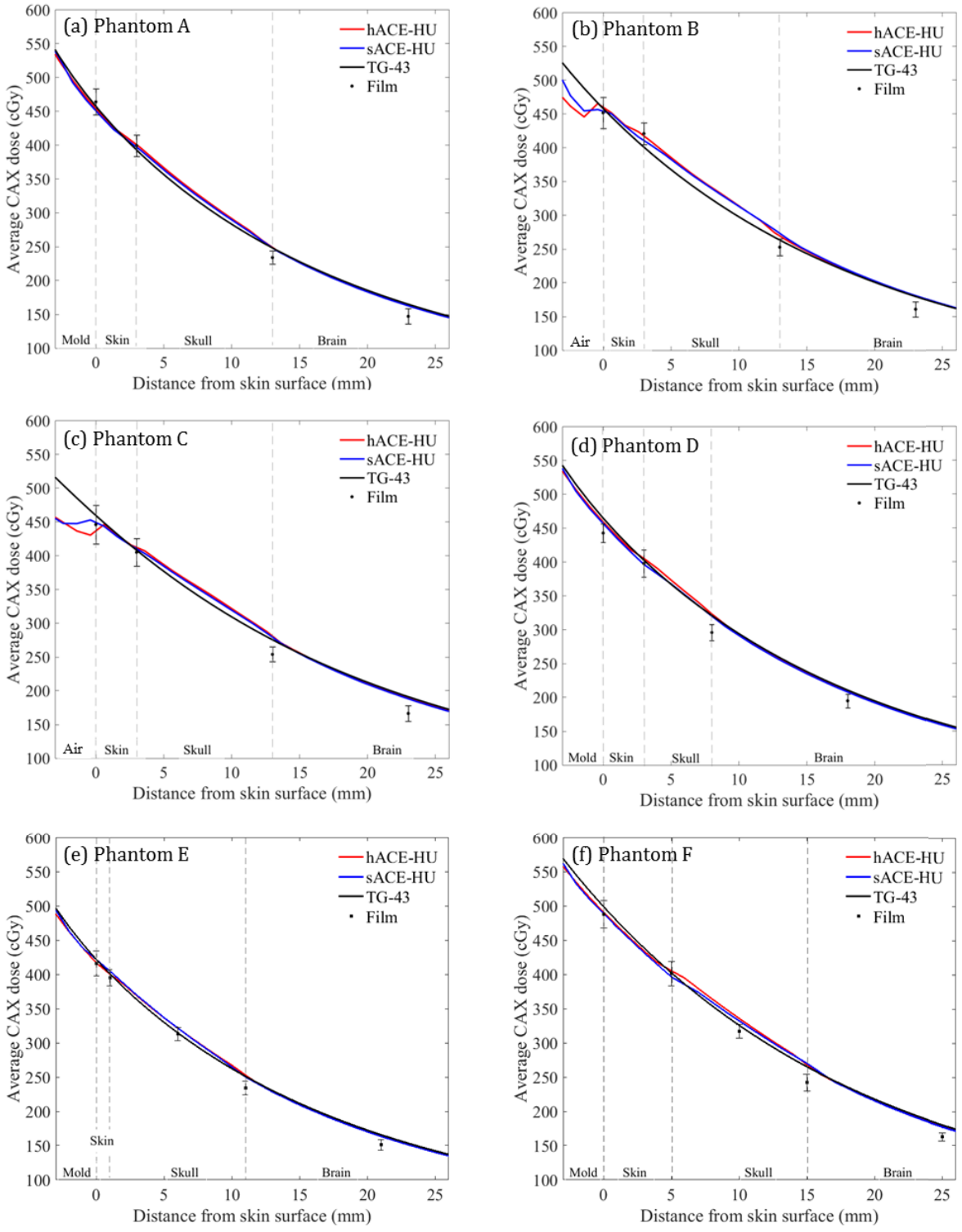

Figure 4.3 – Average CAX dose as calculated by sACE-HU, hACE-HU, and TG-43, and measured by film, for phantoms A (a) through F (f).

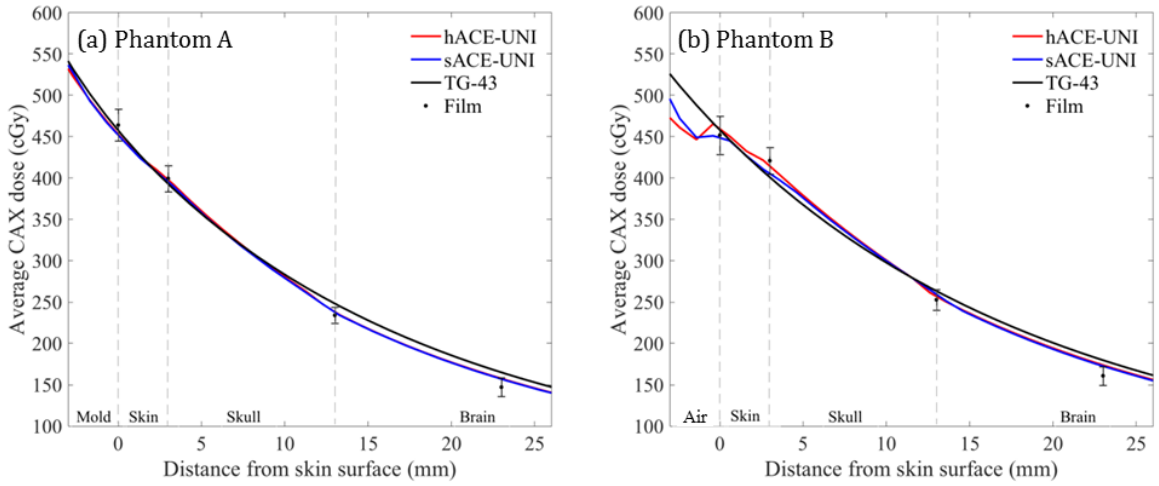

Figure 4.4 – Average CAX dose profiles as calculated by sACE-UNI, hACE-UNI, and TG-43, and measured by film, for phantoms A (a) and B (b).

4.3.2 – Skull Dose

The percent differences between TG-43 ($D_{W,W}$) or hACE calculated dose ($D_{M,M}$) and the skull film dose ($D_{W,M}$) are given in Table 4.5. For phantoms E and F, the difference between the measured and calculated doses is not statistically significant. The TG-43 calculation of $D_{W,W}$ is in better agreement with the film measured $D_{W,M}$ than the hACE calculated $D_{M,M}$.

Table 4.5 – Average percent dose differences between TG-43 calculated doses and skull film measurements, and hACE calculated doses and skull film measurements. Uncertainties are stated with a coverage factor of 2 (k=2).

Phantom	$\Delta D_{film(skull)\text{-}TG43}$ (%)	$\Delta D_{film(skull)\text{-}hACE}$ (%)
E	-1 ± 8	-3 ± 10
F	-3 ± 8	-6 ± 10

4.4 – Discussion

The film measurements and ACE calculations for Phantom W were found to be in good agreement with the TG-43 calculated doses on average for all four film locations. As observed in Figure 4.2,

there is an apparent improved agreement between the average film and TG-43 doses with increasing depth in the phantom, but the percent dose difference (Equation 4.1) does not decrease with increasing depth.

The finely detailed geometry of the human head makes contouring each tissue type (skull, brain, skin etc.) impractical in clinical applications. Therefore, using HU from CT images, rather than assigning uniform densities and attenuation coefficients in OcB, is necessary. Figure 4.3 clearly illustrates that both TG-43 and ACE-HU calculations underestimate the decrease in dose measured below the skull layer. Considering phantoms A and B and the two film locations below the skull layer, TG-43 and hACE-HU overestimate the film dose by $(8 \pm 4)\%$ and $(8 \pm 6)\%$ on average, respectively. In contrast, ACE-UNI overestimates the film dose below the skull layer, for phantoms A and B, by $(4 \pm 6)\%$ on average. Although the agreement is better between film and ACE-UNI compared to film and ACE-HU, the cortical bone material available in OcB has a CT number (1827) significantly higher than the actual CT number (910) of the hard bone equivalent plastic. Therefore, the apparent improvement in accuracy of ACE-UNI does not support the use of uniform densities compared to HU. The ACE-UNI calculations further emphasize that ACE appears to underestimate attenuation of the photon fluence through bone.

As described in Section 2.1.3.3, ACE calculates scatter kernels in water and then scales the kernels according to the average attenuation coefficient for the material being irradiated. ACE does not calculate the scatter kernels in the material itself, which may result in significantly different energy spectra for the scattered photons. Therefore, the scaled scatter kernel for the bone equivalent material may not adequately model the increased photon attenuation and photon absorption, relative to water, or spectral hardening due to preferential attenuation of the lower energy photons (3,4).

The effects of this scaling approximation have been demonstrated with a prostate patient CT data set, where MC calculates doses up to 15% higher in pelvic bone, and lower doses beyond

bone, compared to ACE (5,6). The skull film measurements (in phantoms E and F) of $D_{W,M}$ were found to be within the uncertainty of the TG-43 calculated doses ($D_{W,W}$) and hACE ($D_{M,M}$) calculated doses. Fonseca *et al.* (7) have demonstrated that the large cavity theory conversion factor ($D_{M,M}/D_{W,M}$) is highly dependent on the photon spectrum. Their MC simulations of Ir-192 BT treatments of head and neck cancer, using CT images, yielded a conversion factor in bone of 1.14 at a location past bone and tissue relative to the dwell positions. If the film measurements of $D_{W,M}$ are converted to $D_{M,M}$ using a conversion factor of 1.14, which is justifiable given our measurement geometry, the estimated average dose to bone from the film measurement ($D_{M,M}$) is (11 ± 10)% and (8 ± 10)% greater than the corresponding hACE calculated dose for phantoms E and F, respectively. Therefore, it is expected that hACE underestimates the dose to bone compared to film, which is consistent with the observation that ACE underestimates dose in bone compared to MC.

The TD5/5 and TD5/50 bone dose tolerances presented by Emami *et al.* are 52 Gy and 65 Gy, respectively (8). Others have suggested tolerances for bone marrow of 40 Gy and 50 Gy for TD5/5 and TD50/5, respectively (9). A more recent school of thought considers a bone dose above 60 Gy, to a larger volume, to be concerning due to the increase in probability of fracture (10,11). Underestimating the bone dose would most likely not be of clinical concern for NMSC treatments because the maximum 40 Gy dose, prescribed to the CTV, places the bone dose well within tolerance.

An additional consideration is that the current version of OcB does not allow users to enter CT number to electron density calibration curves for the CT scanners at their clinics. Instead, OcB contains a standard calibration curve. For the HU range corresponding to the slab phantom skull material (800-1000 HU), the OcB electron density is on average (3.0 ± 0.1)% lower than the electron density for the CT scanner at our clinic. Considering the linear attenuation of a "narrow beam" Ir-192 source through 1 cm of bone material, a 3% decrease in electron density would result

in a less than 1% increase in fluence. Therefore, the HU-electron density calibration curve is most likely not causing a substantial error.

4.5 – Conclusion

Comparisons between TG-43 and Oncentra® Brachy ACE v4.5 dose calculations were made using CT images of multiple configurations of a slab phantom that models the tissue layers of a human head. Triple channel film dosimetry was performed to assess the accuracy of the ACE calculations. Above the skull layer, TG-43 and ACE calculations were found to agree with film measurements. With respect to film measurements, TG-43 and ACE calculations were found to overestimate the dose below the skull layer of the phantoms. Once converted to $D_{M,M}$, the skull dose measured by film was most likely greater than that calculated by ACE and TG-43. Therefore, in our work, ACE appeared to underestimate the dose to bone, which has been observed by others through MC simulation. This inaccuracy in the ACE calculations most likely results from the use of approximate photon scatter spectra in non-water material, rather than spectra generated within the material itself. Until this issue is further investigated and resolved, TG-43 represents a better choice for dose calculations involving bone.

4.6 – References

1. Woodard H, White D. The composition of body tissues. Br J Radiol. 1986;59(708):1209–18.

2. White D, Widdowson E, Woodard H, Dickerson J. The composition of body tissues (II). Fetus to young adult. Br J Radiol. 1991;64(758):149–59.

3. Anagnostopoulos G, Baltas D, Karaiskos P, Pantelis E, Papagiannis P, Sakelliou L. An analytical dosimetry model as a step towards accounting for inhomogeneities and bounded geometries in 192Ir brachytherapy treatment planning [Electronic Version]. Phys Med Biol. 2003;48(11):1625–47.

4. Carlsson Tedgren AK, Ahnesjö A. Accounting for high Z shields in brachytherapy using collapsed cone superposition for scatter dose calculation [Electronic Version]. Med Phys. 2003;30(8):2206–17.

5. Ma Y, Lacroix F, Lavallée M-C, Beaulieu L. Validation of the Oncentra Brachy Advanced Collapsed cone Engine for a commercial 192Ir source using heterogeneous geometries [Electronic Version]. Brachytherapy. Elsevier; 2015;14(6):939–52.

6. van Veelen B, Ma Y, Beaulieu L. ACE: Advanced Collapsed cone Engine (White Paper). White Paper Elekta. 2014;1–16.

7. Fonseca GP, Tedgren ÅC, Reniers B, Nilsson J, Persson M, Yoriyaz H, et al. Dose specification for ^{192}Ir high dose rate brachytherapy in terms of dose-to-water-in-medium and dose-to-medium-in-medium [Electronic Version]. Phys Med Biol. 2015;60(11):4565–79.

8. Emami B, Lyman J, Brown A, Coia L, Goitein M, Munzenrider J, et al. Tolerance of normal tissue to therapeutic irradiation [Electronic Version]. Int J Radiat Oncol Biol Phys. 1991;21:109–22.

9. Law R. Frontiers of radiation therapy and oncology. Vaeth J, Meyer J, editors. San Franscisco, CA: Basel:Karger; 1989. 7-40 p.

10. Taremi M, Hope A, Lindsay P, Dahele M, Fung S, Purdie TG, et al. Predictors of radiotherapy induced bone injury (RIBI) after stereotactic lung radiotherapy [Electronic Version]. Radiat Oncol. 2012;7:159.

11. Sargos P, Mamou N, Dejean C, Henriques de Figueiredo B, Huchet A, Italiano A, et al. Dose de tolérance à l'irradiation des tissus sains : l'os chez l'adulte [Electronic Version]. Cancer/Radiothérapie. 2010;14:386–91.

Chapter 5 – Summary and Future Work

5.1 – Summary

In this research work, the performance of ACE was experimentally evaluated for two types of BT cancer treatments: gynecological treatments using a MCVC, and NMSC of the scalp using surface molds. The dose delivered to clinically relevant phantoms was measured using radiochromic film and compared to TG-43 and ACE calculated doses.

The MCVC applicator measurements revealed information about both ACE and the applicator itself. The sACE calculation was found to underestimate an increase in dose above two grooves on the outside of the applicator, which was identified using film measurements to be (11 ± 8)% of the mean dose. This inaccuracy appears to be caused by the larger (2 mm vs. 1 mm) grid calculation size used by sACE at the surface of the applicator. The hACE calculation predicted a (6 ± 8)% increase in dose above the two grooves. Additionally, variable positioning of the source in the central channel of the applicator was the likely cause of an observed background azimuthal variation in dose of (10 ± 4)%.

Radiochromic film measurements were performed in a multi-configuration slab phantom that was designed to model the layers of the human head. Planning was performed using CT images of the phantom, and ACE calculations were performed using HU values from the CT images. The ACE and TG-43 calculations were found to underestimate the attenuation of the photon fluence through the skull layer and therefore overestimate the dose to tissues beyond bone. This underestimation of attenuation through bone has been demonstrated for HDR prostate brachytherapy by others through Monte Carlo simulations (1–3) and is attributed to ACE using scatter spectra generated in water rather than the material itself.

5.2 – Future Work

As presented here and in work reported by others, dose calculations performed using ACE contain inaccuracies that should be addressed before clinical implementation for certain treatments. Once

addressed, ACE should be re-assessed by comparison to Monte Carlo simulations and experimental measurements.

A logical next step for the experimental verification of MBDCAs with radiochromic film would be to develop a "standard phantom" that could be used during commissioning to compare dose calculations and film measurements in the presence of heterogeneities. Moura *et al.* developed a heterogeneous phantom, but it does not investigate air-tissue heterogeneities, and has not been used to investigate ACE (4). Similarly, Palmer *et al.* developed a water equivalent phantom to measure the dose delivered using different gynecological applicators, on orthogonal planes (5).

Verification of ACE calculations, via radiochromic film measurements, could be further performed for metal surface/skin applicators, shielded gynecological applicators, doses at air-skin interfaces (as may occur in breast cancer treatments), or esophageal cancer treatments, which present air and bone heterogeneities. Some work has been done to compare in-vivo radiochromic film measurements to TG-43 (6), and further comparison of in-vivo film measurements to ACE may be informative.

5.3 – References

1. Ma Y, Lacroix F, Lavallée M-C, Beaulieu L. Validation of the Oncentra Brachy Advanced Collapsed cone Engine for a commercial 192Ir source using heterogeneous geometries [Electronic Version]. Brachytherapy. 2015;14(6):939–52.

2. van Veelen B, Ma Y, Beaulieu L. ACE: Advanced Collapsed cone Engine (White Paper). White Paper Elekta. 2014;1–16.

3. Anagnostopoulos G, Baltas D, Karaiskos P, Pantelis E, Papagiannis P, Sakelliou L. An analytical dosimetry model as a step towards accounting for inhomogeneities and bounded geometries in 192Ir brachytherapy treatment planning [Electronic Version]. Phys Med Biol. 2003;48(11):1625–47.

4. Moura ES, Micka J a., Hammer CG, Culberson WS, DeWerd L a., Rostelato MECM, et al. Development of a phantom to validate high-dose-rate brachytherapy treatment planning systems with heterogeneous algorithms [Electronic Version]. Med Phys. 2015;42(4):1566–74.

5. Palmer AL, Lee C, Ratcliffe AJ, Bradley D, Nisbet A. Design and implementation of a film dosimetry audit tool for comparison of planned and delivered dose distributions in high dose rate (HDR) brachytherapy [Electronic Version]. Phys Med Biol. 2013;58(19):6623–40.

6. Pai S, Reinstein LE, Gluckman G, Xu Z, Weiss T. The use of improved radiochromic film for in vivo quality assurance of high dose rate brachytherapy [Electronic Version]. Med Phys. 1998;25(7 Pt 1):1217–21.

Bibliography

1. Delaney G, Jacob S, Featherstone C, Barton M. The role of radiotherapy in cancer treatment: Estimating optimal utilization from a review of evidence-based clinical guidelines [Electronic Version]. Cancer. 2005;104(6):1129–37.
2. Basil H. Brachytherapy, Conquering cancer, The first 100 years. Springfield, VA: Best Cure Foundation, Brachytherapy Research & Educational Foundation; 2014. 1-160 p.
3. Han K, Milosevic M, Fyles A, Pintilie M, Viswanathan AN. Trends in the utilization of brachytherapy in cervical cancer in the United States[Electronic Version]. Int J Radiat Oncol Biol Phys. Elsevier Inc.; 2013;87(1):111–9.
4. Petereit DG, Frank SJ, Viswanathan AN, Erickson B, Eifel P, Nguyen PL, et al. Brachytherapy: Where has it gone [Electronic Version]? J Clin Oncol. 2015;33(9):980–2.
5. Rose JN, McLaughlin PY, Hanna TP, D'Souza D, Sur R, Falkson CB. Surface mold brachytherapy for nonmelanoma skin cancer: Canadian patterns of practice [Electronic Version]. Pract Radiat Oncol. American Society for Radiation Oncology; 2014;4(6):398–403.
6. Hoskin P, Coyle C, editors. Radiotherapy in Practice: Brachytherapy. 2nd ed. New York: Oxford University Press; 2011.
7. ICRU 38. Dose and volume specification for reporting intracavitary therapy in gynecology. ICRU 38. Bethesda, MD; 1985.
8. Van Dyk J, editor. The modern technology of radiation oncology: a compendium for medical physicists and radiation oncologists. Madison, WI: Medical Physics Publishing; 1999.

9. Ye S-J, Brezovich IA, Shen S, Duan J, Popple RA, Pareek PN. Attenuation of intracavitary applicators in 192Ir-HDR brachytherapy [Electronic Version]. Med Phys. 2004;31(7):2097–106.

10. Rodríguez ML, deAlmeida CE. Absorbed dose calculations in a brachytherapy pelvic phantom using the Monte Carlo method [Electronic Version]. J Appl Clin Med Phys. 2002;3(4):285–92.

11. Meigooni A, Nath R. Tissue inhomogeneity correction for brachytherapy sources in a heterogeneous phantom with cylindrical symmetry [Electronic Version]. Med Phys. 1991;19(2):401–7.

12. Chandola RM, Tiwari S, Kowar MK, Choudhary V. Effect of inhomogeneities and source position on dose distribution of Nucletron high dose rate Ir-192 brachytherapy source by Monte Carlo simulation [Electronic Version]. J Cancer Res Ther. 2010;6(1):54–7.

13. van Veelen B, Ma Y, Beaulieu L. ACE: Advanced Collapsed cone Engine (White Paper). White Paper Elekta. 2014;1–16.

14. Varian Medical Systems. BrachyVision ™ Acuros ™ Advanced brachytherapy dose calculations (brochure). Palo Alto. 2009;

15. Carlsson Tedgren AK, Ahnesjö A. Accounting for high Z shields in brachytherapy using collapsed cone superposition for scatter dose calculation [Electronic Version]. Med Phys. 2003;30(8):2206–17.

16. Ahnesjö A. Collapsed cone convolution of radiant energy for photon dose calculation in heterogeneous media [Electronic Version]. Med Phys. 1989;16(4):577–92.

17. Carlsson AK, Ahnesjö A. The collapsed cone superposition algorithm applied to scatter dose calculations in brachytherapy [Electronic Version]. Med Phys. 2000;27(10):2320–32.

18. Vassiliev ON, Wareing TA, McGhee J, Failla G, Salehpour MR, Mourtada F. Validation of a new grid-based Boltzmann equation solver for dose calculation in radiotherapy with photon beams [Electronic Version]. Phys Med Biol. 2010;55(3):581–98.

19. Mikell JK, Mourtada F. Dosimetric impact of an 192Ir brachytherapy source cable length modeled using a grid-based Boltzmann transport equation solver [Electronic Version]. Med Phys. 2010;37(9):4733–43.

20. Lewis E, Miller W. Computational methods of neutron transport. New York, NY, Wiley; 1984.

21. Beaulieu L, Carlsson Tedgren A, Carrier J-F, Davis SD, Mourtada F, Rivard MJ, et al. Report of the Task Group 186 on model-based dose calculation methods in brachytherapy beyond the TG-43 formalism: Current status and recommendations for clinical implementation [Electronic Version]. Med Phys. 2012;39(10):6208.

22. Papagiannis P, Pantelis E, Karaiskos P. Current state of the art brachytherapy treatment planning dosimetry algorithms. Br J Radiol [Internet]. 2014;87(1041):20140163. Available from: http://www.birpublications.org/doi/abs/10.1259/bjr.20140163

23. Zourari K, Major T, Herein A, Peppa V, Polgár C, Papagiannis P. A retrospective dosimetric comparison of TG43 and a commercially available MBDCA for an APBI brachytherapy patient cohort. Phys Medica [Internet]. 2015;1–8. Available from: http://linkinghub.elsevier.com/retrieve/pii/S1120179715001209

24. Zourari K, Pantelis E, Moutsatsos A, Sakelliou L, Georgiou E, Karaiskos P, et al. Dosimetric accuracy of a deterministic radiation transport based 192Ir brachytherapy treatment planning system. Part III [Electronic Version]. Comparison to Monte Carlo simulation in voxelized anatomical computational models. Med Phys. 2013;40(1):011712.

25. Petrokokkinos L, Zourari K, Pantelis E, Moutsatsos a, Karaiskos P, Sakelliou L, et al. Dosimetric accuracy of a deterministic radiation transport based 192Ir brachytherapy treatment planning system. Part II: Monte Carlo and experimental verification of a multiple source dwell position plan employing a shielded applicator [Electronic Version]. Med Phys. 2011;38(4):1981–92.

26. Johns HE, Cunningham JR. The physics of radiology. 4th ed. Springfield, IL: Charles C Thomas; 1983.

27. Podgorsak EB. Radiation physics for medical physicists. 2nd ed. Heidelberg, Germany: Springer; 2010.

28. Nath R, Anderson LL, Luxton G, Weaver KA, Williamson JF, Meigooni AS. Report of AAPM Radiation Therapy Committee Task Group 43: Dosimetry of Interstitial Brachytherapy Sources [Electronic Version]. Med Phys. 1995;22(2):209–34.

29. Rivard MJ, Coursey BM, DeWerd LA, Hanson WF, Huq MS, Ibbott GS, et al. Update of AAPM Task Group No. 43 Report: A revised AAPM protocol for brachytherapy dose calculations [Electronic Version]. Med Phys. 2004;31(3):633–74.

30. Venselaar J, Meigooni AS, Baltas D, Hoskin P, editors. Comprehensive brachytherapy: physical and clinical aspects. Boca Raton, FL: CRC Press, Taylor and Francis Group;

31. Williamson JF, Li Z. Monte Carlo aided dosimetry of the microselectron pulsed and high dose-rate 192Ir sources [Electronic Version]. Med Phys. 1995;22(6):809–19.

32. Daskalov GM, Loffler E, Williamson JF. Monte Carlo-aided dosimetry of a new high dose-rate brachytherapy source [Electronic Version]. Med Phys. 1998;25(11):2200–8.

33. Granero D, Vijande J, Ballester F, Rivard MJ. Dosimetry revisited for the HDR 192Ir brachytherapy source model mHDR-v2 [Electronic Version]. Med Phys. 2011;38(1):487–94.

34. Carlsson AK, Ahnesjö A. The collapsed cone superposition algorithm applied to scatter dose calculations in brachytherapy [Electronic Version]. Med Phys. 2000;27(10):2320–32.

35. Carlsson Tedgren AK, Ahnesjö A. Accounting for high Z shields in brachytherapy using collapsed cone superposition for scatter dose calculation [Electronic Version]. Med Phys. 2003;30(8):2206–17.

36. DeWerd LA, Ibbott GS, Meigooni AS, Mitch MG, Rivard MJ, Stump KE, et al. A dosimetric uncertainty analysis for photon-emitting brachytherapy sources: report of AAPM Task Group No. 138 and GEC-ESTRO [Electronic Version]. Med Phys. 2011;38(2):782–801.

37. Zourari K, Pantelis E, Moutsatsos A, Sakelliou L, Georgiou E, Karaiskos P, et al. Dosimetric accuracy of a deterministic radiation transport based 192Ir brachytherapy treatment planning system. Part III. Comparison to Monte Carlo simulation in voxelized anatomical computational models [Internet Version]. Med Phys. 2013;40(1):11712.

38. Ballester F, Carlsson Tedgren Å, Granero D, Haworth A, Mourtada F, Fonseca GP, et al. A generic high-dose rate 192Ir brachytherapy source for evaluation of model-based dose calculations beyond the TG-43 formalism [Internet Version]. Med Phys. 2015;42(6):3048–62.

39. Beaulieu L, Carlsson Tedgren A, Carrier J-F, Davis SD, Mourtada F, Rivard MJ, et al. Report of the Task Group 186 on model-based dose calculation methods in brachytherapy beyond the TG-43 formalism: Current status and recommendations for clinical implementation [Electronic Version]. Med Phys. 2012;39(10):6208.

40. Moura ES, Micka JA, Hammer CG, Culberson WS, DeWerd LA, Rostelato MECM, et al. Development of a phantom to validate high-dose-rate brachytherapy treatment planning

systems with heterogeneous algorithms [Electronic Version]. Med Phys. 2015;42(4):1566–74.

41. Sharma R, Jursinic PA. In vivo measurements for high dose rate brachytherapy with optically stimulated luminescent dosimeters [Electronic Version]. Med Phys. 2013;40(7):71730.

42. Petrokokkinos L, Moutsatsos A, Karaiskos P, Kouridou V, Pantelis E, Papagiannis P, et al. On the use of VIP gel dosimetry in HDR brachytherapy [Electronic Version]. J Phys Conf Ser. 2009;164:12051.

43. Subhalaxmi M, Selvam TP. Monte Carlo-based investigation of absorbed-dose energy dependence of radiochromic films in high energy brachytherapy dosimetry [Electronic Version]. J Appl Clin Med Phys. 2014;15(1):4448.

44. Sutherland J. Monte Carlo calculated absorbed-dose energy dependence of EBT and EBT2 film [Electronic Version]. Med Phys. 2010;37(3):1110–6.

45. Massillon-JL G, Chiu-Tsao S-T, Domingo-Muñoz I, Chan MF. Energy Dependence of the New Gafchromic EBT3 Film: Dose Response Curves for 50 KV, 6 and 15 MV X-Ray Beams [Electronic Version]. Int J Med Physics,Clinical Eng Radiat Oncol. 2012;1(2):60–5.

46. Niroomand-Rad A, Blackwell CR, Coursey BM, Gall KP, Galvin JM, Mclaughlin WL, et al. Radiochromic film dosimetry: recommendations of AAPM radiation therapy committee task group no. 55 [Electronic Version]. Med Phys. 1998;25(11).

47. Rink A. Point-based ionizing radiation dosimetry using radiochromic materials and a fiberoptic readout system. Vol. 1, Ph.D Thesis. University of Toronto, Canada; 2008.

48. Lewis D, Micke A, Yu X, Chan MF. An efficient protocol for radiochromic film dosimetry combining calibration and measurement in a single scan [Electronic Version]. Med Phys. 2012;39(10):6339.

49. Ramos Garcia LI, Perez Azorin JF. Improving the calibration of radiochromic films by the use of uncertainties in optical density and dose [Electronic Version]. Med Phys. 2013;40(7).

50. Micke A, Lewis DF, Yu X. Multichannel film dosimetry with nonuniformity correction [Electronic Version]. Med Phys. 2011;38(5):2523–34.

51. Galantai A. The theory of Newton ’s method [Electronic Version]. J Comput Appl Math. 2000;124:25–44.

52. Taylor BN, Kuyatt CE. NIST Technical Note 1297 1994 Edition, Guidelines for Evaluating and Expressing the Uncertainty of NIST Measurement Results. National Institute of Standards and Technology. 1994.

53. Morrison H, Menon G, Sloboda RS. Radiochromic film calibration for low-energy seed brachytherapy dose measurement [Electronic Version]. Med Phys. 2014;41(7):72101.

54. Chiu-Tsao S-T, Medich D, Munro J. The use of new GAFCHROMIC EBT film for 125I seed dosimetry in Solid Water phantom [Electronic Version]. Med Phys. 2008;35(8):3787–99.

55. Goorley T, James M, Booth T, Brown F, Bull J, Cox LJ. Initial MCNP6 Release Overview. Nucl Technol. 2012;180:298–315.

56. Granero D, Vijande J, Ballester F, Rivard MJ. Dosimetry revisited for the HDR 192Ir brachytherapy source model mHDR-v2 [Electronic Version]. Med Phys. 2011;38(1):487–94.

57. Onal C, Guler O, Dolek Y. The impact of air pockets around the vaginal cylinder on vaginal vault brachytherapy [Electronic Version]. Br J Radiol. 2015;88(1047):20140694.

58. Hassauna A, Abdulaziz Bahadur Y, Constantinescu C. Assessment of air pockets in high-dose-rate vaginal cuff brachytherapy using cylindrical applicators [Electronic Version]. J Contemp Brachytherapy. 2014;6(3):271–5.

59. Richardson S, Palaniswaamy G, Grigsby P. Dosimetric effects of air pockets around high-dose rate brachytherapy vaginal cylinders [Electronic Version]. Int J Radiat Oncol Biol Phys. 2010;78(1):276–9.

60. Maxwell A, Thiruthaneeswaran N, Lowe G, Wills R, Sripali S, Hoskin PJ. The Dosimetric Impact of Air in Vaginal Vault Brachytherapy [Electronic Version]. Brachytherapy. Elsevier Inc; 2016;15(2016):S104.

61. Woodard H, White D. The composition of body tissues. Br J Radiol. 1986;59(708):1209–18.

62. White D, Widdowson E, Woodard H, Dickerson J. The composition of body tissues (II). Fetus to young adult. Br J Radiol. 1991;64(758):149–59.

63. Anagnostopoulos G, Baltas D, Karaiskos P, Pantelis E, Papagiannis P, Sakelliou L. An analytical dosimetry model as a step towards accounting for inhomogeneities and bounded geometries in 192Ir brachytherapy treatment planning [Electronic Version]. Phys Med Biol. 2003;48(11):1625–47.

64. Carlsson Tedgren AK, Ahnesjö A. Accounting for high Z shields in brachytherapy using collapsed cone superposition for scatter dose calculation [Electronic Version]. Med Phys. 2003;30(8):2206–17.

65. Ma Y, Lacroix F, Lavallée M-C, Beaulieu L. Validation of the Oncentra Brachy Advanced Collapsed cone Engine for a commercial 192Ir source using heterogeneous geometries [Electronic Version]. Brachytherapy. Elsevier; 2015;14(6):939–52.

66. Fonseca GP, Tedgren ÅC, Reniers B, Nilsson J, Persson M, Yoriyaz H, et al. Dose specification for ^{192}Ir high dose rate brachytherapy in terms of dose-to-water-in-medium and dose-to-medium-in-medium [Electronic Version]. Phys Med Biol. 2015;60(11):4565–79.

67. Emami B, Lyman J, Brown A, Coia L, Goitein M, Munzenrider J, et al. Tolerance of normal tissue to therapeutic irradiation [Electronic Version]. Int J Radiat Oncol Biol Phys. 1991;21:109–22.

68. Law R. Frontiers of radiation therapy and oncology. Vaeth J, Meyer J, editors. San Franscisco, CA: Basel:Karger; 1989. 7-40 p.

69. Taremi M, Hope A, Lindsay P, Dahele M, Fung S, Purdie TG, et al. Predictors of radiotherapy induced bone injury (RIBI) after stereotactic lung radiotherapy [Electronic Version]. Radiat Oncol. 2012;7:159.

70. Sargos P, Mamou N, Dejean C, Henriques de Figueiredo B, Huchet A, Italiano A, et al. Dose de tolérance à l'irradiation des tissus sains : l'os chez l'adulte [Electronic Version]. Cancer/Radiothérapie. 2010;14:386–91.

71. Anagnostopoulos G, Baltas D, Karaiskos P, Pantelis E, Papagiannis P, Sakelliou L. An analytical dosimetry model as a step towards accounting for inhomogeneities and bounded geometries in 192Ir brachytherapy treatment planning [Electronic Version]. Phys Med Biol. 2003;48(11):1625–47.

72. Moura ES, Micka JA, Hammer CG, Culberson WS, DeWerd LA, Rostelato MECM, et al. Development of a phantom to validate high-dose-rate brachytherapy treatment planning systems with heterogeneous algorithms [Electronic Version]. Med Phys. 2015;42(4):1566–74.

73. Palmer AL, Lee C, Ratcliffe AJ, Bradley D, Nisbet A. Design and implementation of a film dosimetry audit tool for comparison of planned and delivered dose distributions in high dose rate (HDR) brachytherapy [Electronic Version]. Phys Med Biol. 2013;58(19):6623–40.

74. Pai S, Reinstein LE, Gluckman G, Xu Z, Weiss T. The use of improved radiochromic film for in vivo quality assurance of high dose rate brachytherapy [Electronic Version]. Med Phys. 1998;25(7 Pt 1):1217–21.

75. Perez-Calatayud J, Ballester F, Das RK, DeWerd LA, Ibbott GS, Meigooni AS, et al. Dose calculation for photon-emitting brachytherapy sources with average energy higher than 50 keV: Report of the AAPM and ESTRO [Electronic Version]. Med Phys. 2012;39(5):2904-2929.

Appendix

The documentation obtained for the permission to reprint the published figures in Figures 2.2 and 2.5 is given below.

AMERICAN ASSOCIATION of PHYSICISTS IN MEDICINE

Angela R. Keyser
Executive Director
akeyser@aapm.org
571.298.1285

DATE OF REQUEST: September 22/2016

FROM:
Brie Cawston-Grant
11560 University Avenue NW, Edmonton, AB, T6G 1Z2

EMAIL ADDRESS: cawstong@ualberta.ca

1. **Permission is granted to:**

   Brie Cawston-Grant (graduate student), University of Alberta

2. **Permission is requested to use the following material:**

   1.) Asa K. Carlsson et al./The collapsed cone superposition algorithm applied to scatter dose calculations in brachytherapy/Medical Physics/Vol. 27/Issue 10/page 2321/2000/Figure 1

   2.) Georgi M. Daskalov et al./Monte Carlo-aided dosimetry of a new high dose-rate brachytherapy source/Medical Physics/Vol. 25/Issue 11/page 2201/1998/Figure 1

   3.) Domingo Granero et al./Dosimetry revisited for the HDR Ir-192 brachytherapy source model mHDR-v2/Medical Physics/Vol. 38/Issue 1/page 488/2011/Figure 1

3. **For what purpose:**
   I would like to use these three images in my Master's Thesis. I am attending the University of Alberta for my master's.

Authors seeking permission must also notify the first author of the article from which permission is being sought.

Permission is hereby granted: Angela R. Keyser — **Signature**

September 23/2016 — **Date**

The Association's Journals are Medical Physics and Journal of Applied Medical Physics
Member Society of the American Institute of Physics and the International Organization of Medical Physics

1631 Prince Street | Alexandria, VA 22314-2818 | phone 571.298.1300 | fax 571.298.1301 | www.aapm.org